

## Nonlinear oscillations and collapse of elongated bubbles subject to weak viscous effects

Kostas Tsigliffis<sup>a)</sup> and Nikos A. Pelekasis<sup>b)</sup>

*Department of Mechanical and Industrial Engineering, University of Thessaly, Volos 38334, Greece*

(Received 20 December 2004; accepted 19 August 2005; published online 4 October 2005)

The weak viscous oscillations of a bubble are examined, in response to an elongation that perturbs the initial spherical shape at equilibrium. The flow field in the surrounding liquid is split in a rotational and an irrotational part. The latter satisfies the Laplacian and can be obtained via an integral equation. A hybrid boundary-finite element method is used in order to solve for the velocity potential and shape deformation of axisymmetric bubbles. Weak viscous effects are included in the computations by retaining first-order viscous terms in the normal stress boundary condition and satisfying the tangential stress balance. An extensive set of simulations was carried out until the bubble either returned to its initial spherical shape, or broke up. For a relatively small initial elongation the bubble returned to its initial spherical state regardless of the size of the Ohnesorge number;  $Oh = \mu / (\rho R \sigma)^{1/2}$ . For larger initial elongations there is a threshold value in  $Oh^{-1}$  above which the bubble eventually breaks up giving rise to a “donut” shaped larger bubble and a tiny satellite bubble occupying the region near the center of the original bubble. The latter is formed as the round ends of the liquid jets that approach each other from opposite sides along the axis of symmetry, coalesce. The size of the satellite bubble decreased as the initial elongation or  $Oh^{-1}$  increased. This pattern persisted for a range of large initial deformations with a decreasing threshold value of the  $Oh^{-1}$  as the initial deformation increased. As its equilibrium radius increases the bubble becomes more susceptible to the above collapse mode. The effect of initial bubble overpressure was also examined and it was seen that small initial overpressures, for the range of initial bubble deformations that was investigated, translate the threshold of  $Oh^{-1}$  to larger values while at the same time increasing the size of the satellite bubble. © 2005 American Institute of Physics.

[DOI: [10.1063/1.2083947](https://doi.org/10.1063/1.2083947)]

### I. INTRODUCTION

Bubble oscillations and collapse has been a field of research since the early twentieth century when Lord Rayleigh<sup>1</sup> first studied the spontaneous generation and collapse of bubbles, in an effort to explain the damage of propellers of high speed boats and submarines. He described the process of cavitation in which bubbles are generated as a result of changes in the local pressure field. Such bubbles can oscillate quite violently and subsequently collapse and damage the propeller's surface. This is a spherically symmetric type of collapse that is predicted by the well-known Rayleigh-Plesset equation<sup>2</sup> and is associated with the emission of sound during its last stages.

Alternatively, it is possible to trigger bubble oscillations through the use of a short laser pulse<sup>3</sup> that is focused into the liquid. In this fashion, heating of impurities and/or dielectric breakdown takes place generating a plasma spot, which subsequently expands to form a cavity. Depending on the duration of the pulse bubbles with sizes ranging from micro to millimeters are produced.<sup>4</sup> Due to the geometry and the energy intensity of the laser pulse<sup>4</sup> millimeter-sized bubbles initially assume an almost spherical shape whereas

micrometer-sized bubbles are initially elongated. In both cases a significant overpressure is acquired, relative to the internal pressure necessary to support a spherical bubble of the same volume in a fluid with the same static pressure in the far field. The latter is considered as the equilibrium state of the bubble over which a combination of disturbances is imposed, namely an initial elongation and pressurization, upon application of the laser pulse. The bubble starts oscillating quite intensively, depending on the magnitude of the disturbance, and eventually collapses. For relatively large bubbles (equilibrium radius in the order of millimeters), this process is characterized by almost spherical shapes; it is accompanied by light emission and the entire phenomenon is called single bubble sonoluminescence. Smaller bubbles collapse asymmetrically and have not been observed to emit light during collapse.<sup>4</sup> Since its discovery single-bubble sonoluminescence has evoked a number of research efforts both along the lines of experimental investigation and modeling, in order to reveal the underlined hydrodynamical aspects of the phenomenon and their association with the properties of the emitted light. According to the most widely accepted theory during the last stages of collapse a shock wave is produced that is traveling both outwards into the fluid and inwards toward the center of the cavity.<sup>3</sup> However, in order for this mechanism to be valid a certain degree of sphericity is required for the bubble shape during collapse.

<sup>a)</sup>Electronic mail: [kotsigl@uth.gr](mailto:kotsigl@uth.gr)

<sup>b)</sup>Author to whom correspondence should be addressed. Telephone: 30-24210-74102. Fax: 30-24210-74050. Electronic mail: [pe1@uth.gr](mailto:pe1@uth.gr)

Consequently, it is of great importance to identify the mode of collapse for laser-induced bubbles oscillating under conditions similar to those pertaining to sonoluminescence experiments.

In a different context, it is of interest to investigate the possibility that during bubble collapse or breakup universalities exist that may or may not be of the same nature as those obtained in the case of capillary pinch-off of initially elongated inviscid drops.<sup>5,6</sup> Clearly, the existence of volume oscillations in the case of bubbles complicates the dynamics and the initial energy allocation between the breathing mode and higher modes corresponding to shape deformation will play an important role in the long-time behavior of the bubble. As will be seen in the following sections, for small initial overpressures and moderate initial elongations bubble breakup will occur when the inverse Ohnesorge number,  $Oh = \mu / (R\sigma\rho)^{1/2}$ , based on the bubble size, surface tension, and liquid viscosity, becomes larger than a threshold value. Ohnesorge,  $Oh$ , is a dimensionless number that measures the relative importance of viscous and surface tension forces. For axisymmetric bubbles with fore-aft symmetry, during breakup two countercurrent jets are formed on either side of the axis of symmetry connecting the two poles, that impinge upon each other on the equatorial plane which is also a plane of symmetry in this case. During the final stages of the breakup process the relevant time and space scales at this stage of the motion do not depend on the initial conditions of the problem and seem to obey the same universal law that governs capillary pinch-off of elongated drops. More details are given in the results and discussion section of this article.

As a first step towards simulating laser induced bubbles, the present study will focus on the breakup process of bubbles that are initially elongated along their axis of symmetry. The amount of initial overpressure is assumed to be either vanishing or small. In this fashion an effort will also be made to examine the dynamics of bubble collapse for possible universalities.

In Sec. II the governing equations of the problem are presented. The motion is decomposed in an irrotational part that is described via a boundary-integral representation,<sup>7</sup> Sec. II A, and in a rotational part that is described via a boundary layer approach that is valid for weak viscous effects,<sup>8</sup> Sec. II B. In Sec. II C the variation of the total energy of the system is obtained including the effect of dissipation, and is used as an integral check on the accuracy of our calculations. Next, the numerical solution of the problem is presented and convergence tests along with validation tests are given in Sec. III. In Sec. IV an extensive account of the results that were obtained numerically is presented and the effect of the basic parameters is discussed. Bubbles possessing fore-aft symmetry along the symmetry axis are examined and their long-term dynamic state is calculated as a function of the initial elongation,  $S$ , and the Ohnesorge number,  $Oh$ . Micrometer-sized bubbles are investigated and this size is reflected in the dimensionless static pressure in the far-field,  $P_{St}' = P_{St}' / (2\sigma/R)$ , as well as in  $Oh$ ;  $R$  is the radius of a spherical bubble with the same volume as the initial volume of the elongated bubble,  $P_{St}'$  is the far field pressure taken to be equal to the atmospheric pressure,  $\rho$  and  $\mu$  denote the

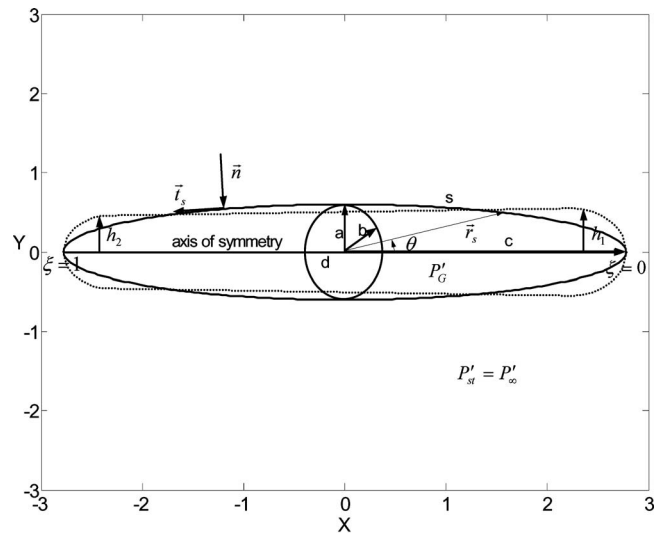


FIG. 1. Initial shape of the bubble for the symmetric (—) and the asymmetric (---) case.

density and viscosity, respectively, of the surrounding fluid and  $\sigma$  denotes the interfacial tension. The air-water system is examined. For micrometer-sized bubbles oscillating in water  $Oh^{-1} \sim 20.5$ . Nevertheless,  $Oh$  is varied over a wide range in order to assess the effect of viscous dissipation. The effect of small internal overpressures as well as that of initial asymmetries is also presented. Finally, in Sec. V the results are discussed in the context of previous studies and directions for future research are suggested.

## III. PROBLEM FORMULATION

We want to investigate the nonlinear oscillations of a bubble that is initially elongated along its axis of symmetry from its spherical shape with radius  $R$  at static equilibrium, Fig. 1. The interior pressure,  $P'_G$ , may be simultaneously increased but the magnitude of the disturbance,  $\epsilon_B$ , will remain small in the context of this study:

$$P'_G(t=0) = P'_G(t=0_-)(1 + \epsilon_B). \quad (1)$$

It should be noted that throughout this study primed letters denote dimensional variables. In the absence of any acoustic disturbances,  $\epsilon=0$ , and the pressure in the far field acquires its static value,  $P'_{St}$ ,

$$P'_\infty = P'_{St}(1 + \epsilon \cos \omega'_f t), \quad (2)$$

with  $\omega'_f$  denoting the dimensional forcing frequency of the disturbance. At equilibrium the fluid surrounding the bubble is quiescent and the pressure inside the bubble is connected to that in the far field via the Young-Laplace equation,

$$P'_G(t=0_-) - P'_{St} = \frac{2\sigma}{R}. \quad (3)$$

The shape of the bubble is assumed to be axisymmetric at all times while the disturbed shape at  $t=0$  is characterized by fore-aft symmetry with respect to the equatorial plane, in most of the cases examined. In fact, we assume that the disturbed shape is that of an ellipsoid

$$\frac{x'^2}{a^2} + \frac{y'^2}{b^2} + \frac{z'^2}{c^2} = 1 \quad (4)$$

with two equal semiaxes,  $a=b$ , in the equatorial plane,  $x'y'$ , and the third one,  $c$ , along the axis of symmetry,  $z'$ , characterizing the extend of an initial elongation. For a given initial volume,  $V_0$ , of the disturbed bubble we can calculate through the following relationships for the volume of a spherical and an ellipsoidal object, the equivalent radius  $R$  and the ratio  $c/R$  as a function of  $S=a/R$ , which is a parameter that will be used as a means to control the magnitude of initial elongation:

$$V_0 = \frac{4}{3}\pi R^3 = \frac{4}{3}\pi a^2 c \rightarrow R = \left(\frac{3V_0}{4\pi}\right)^{1/3}, \quad (5)$$

$$\frac{c}{R} = \frac{1}{(a/R)^2} = \frac{1}{S^2}.$$

After introducing spherical coordinates,

$$x' = r' \sin \theta \cos \phi, \quad y' = r' \sin \theta \sin \phi, \quad z' = r' \cos \theta \quad (6)$$

in Eq. (4) we obtain the following equation describing the initial shape of the bubble:

$$r = f(\theta, t=0) = \frac{S}{\sqrt{S^6 \cos^2 \theta + \sin^2 \theta}}, \quad (7)$$

where the azimuthal angle  $\phi$  is set to zero without any loss of generality due to axisymmetry, and  $r=r'/R$ . When  $S=1$  we recover the spherical shape whereas as  $S$  decreases the imposed elongation along the axis of symmetry becomes stronger. Nevertheless, the model presented here allows for asymmetric shapes as well. Such shapes are obtained by constructing an axisymmetric body consisting of two hemispheres that are attached on each one of the poles and are connected in the middle section of the body by a cone with variable radius. For a given volume, i.e., fixed  $R$ , and total initial elongation,  $\ell=2c/R$ , we use the ratio between the radii of the two hemispheres,  $k=h_1/h_2$ , as a parameter controlling the degree of asymmetry. Thus, it can be easily shown that the ratio,  $s$ , between the radius,  $h_2$ , of the cone's smaller hemisphere and  $R$ , is related to  $\ell$  and  $k$  through the expression

$$\ell = \frac{4 - 2s^3 \cdot (k^3 + 1) + s^3(k+1)(k^2 + k + 1)}{s^2(k^2 + k + 1)}, \quad (8)$$

which uniquely determines the shape of the body (see also Fig. 1). Having determined the initial geometry of the bubble the interior overpressure can be estimated provided the energy level of the laser pulse is known, possibly from experimental investigations. In this article we will assume small overpressure levels which amounts to small values of parameter  $\varepsilon_B$ .

The dynamics of a bubble subjected to the kind of disturbances presented above is normally described through the use of potential theory. If, however, one has to model situations with bubble sizes in the order of micrometers, then

viscosity becomes the dominant dissipation mechanism and has to be accounted for. For bubbles oscillating in water with equilibrium radii ranging between 10 and 1000  $\mu\text{m}$  the inverse Ohnesorge number varies, roughly, between 30 and 1000. This is the range of  $\text{Oh}^{-1}$  within which a theory that takes into account weak viscous effects would be applicable, provided there is no large-scale separation taking place in the liquid boundary layer surrounding the bubble's surface.

The equivalent radius  $R$  is assigned as the characteristic length of the problem thus giving,  $r=r'/R$ ,  $f=f'/R$ , as the dimensionless distance from the origin of the spherical coordinate system and dimensionless location of the interface, respectively. In the absence of a characteristic velocity, surface tension is used in order to render velocity, pressure and time dimensionless,  $V=V'/(c/R/\rho)^{1/2}$ ,  $p=p'/(2\sigma/R)$ ,  $t=t'/(cR^3/\sigma)^{1/2}$ . Considering incompressible flow the dimensionless equations governing the motion in the ambient fluid and the deformation of the bubble read as follows: continuity equation expressing the differential mass balance,

$$\nabla \cdot V = 0; \quad (9)$$

Navier-Stokes equations expressing the differential linear momentum balance

$$\frac{\partial V}{\partial t} + V \cdot \nabla V = -2 \nabla P + \text{Oh} \nabla^2 V, \quad (10)$$

where the effect of gravity is dropped due to the small size of the bubbles; kinematic condition forcing points on the surface to move with the fluid velocity

$$r = r_s; \quad \frac{dr_s}{dt} = V, \quad (11)$$

where  $r_s$  denotes the position vector of a material point on the surface of the bubble; force balance on the interface,

$$r = r_s; \quad -P_G n - (-2P\underline{\underline{I}} + \text{Oh}\underline{\underline{T}}) \cdot n = 2Hn = (-\nabla_s \cdot n)n, \quad (12)$$

where  $n$  denotes the outwards pointing unit normal vector with respect to the fluid surrounding the bubble,  $\nabla_s, H$ , denote the surface gradient and mean curvature on the bubble's interface, respectively, and  $\underline{\underline{I}}, \underline{\underline{T}} = \partial V_i / \partial x_j + \partial V_j / \partial x_i$ , the unit and deviatoric stress tensor, respectively; quiescent flow conditions in the far field,

$$r \rightarrow \infty: V \rightarrow 0, \quad (13a)$$

$$P \rightarrow P_\infty = P_{St}. \quad (13b)$$

Due to negligible density and kinematic viscosity of the gas inside the bubble we take the bubble pressure to be uniform and drop the deviatoric part of the stress tensor on the side of the gas inside the bubble. In addition, owing to the very short time frame over which the phenomena that are investigated in the present study evolve, we can neglect heat transfer to and from the surrounding liquid, to a first approximation, and consider adiabatic oscillations. Consequently the variation of the bubble pressure with time is given by

$$P_G(t=0) \left( \frac{4}{3} \pi \right)^\gamma = P_G(t) V_G^\gamma(t), \quad (14)$$

where  $\gamma$  denotes the polytropic constant,  $1 \leq \gamma \leq 1.4$ , and  $V_G$  the dimensionless instantaneous volume of the bubble; for an adiabatic process  $\gamma=1.4$ .

In order to capture the effect of viscosity for relatively large  $\text{Oh}^{-1}$  we first decompose the velocity and pressure fields in an irrotational and a rotational part,

$$V = u + U, \quad (15)$$

$$P = p_{\text{ir}} + p, \quad (16)$$

where

$$u = \nabla \Phi, \quad (17a)$$

$$U = \nabla \times A, \quad (17b)$$

with  $\nabla \times u = 0, \nabla \cdot A = 0$ ; it can be seen that a decomposition of this type is possible for any flow field without any loss in generality.<sup>9</sup> When the flow is characterized by axial symmetry the vector potential is of the form

$$A = A(r, \theta) e_\phi, \quad (18)$$

where  $e_\phi$  is the unit vector in the azimuthal direction. Next we present the formulation for the scalar,  $\Phi$ , and vector potential,  $A$ .

### A. Irrotational flow field

Introducing decomposition (15) in the continuity equation we obtain, using (17a) and (17b),

$$\nabla \cdot u + \nabla \cdot (\nabla \times A) = 0 \rightarrow \nabla^2 \Phi = 0. \quad (19)$$

Thus we recover the well-known result that the scalar velocity potential satisfies the Laplacian. In an effort to capture more complicated bubble shapes for which the Eulerian description would be multivalued, we adopt the Lagrangian formulation for the description of the motion of particles occupying the bubble's interface. As the irrotational pressure and velocity fields must satisfy Bernoulli's equation, the latter can be combined with the normal force balance in the absence of viscous dissipation,

$$2P_G - 2p_{\text{ir}} = 2H, \quad (20)$$

to give the dynamic condition describing the evolution of the velocity potential on the bubble's surface,

$$\frac{D\Phi}{Dt} = \frac{1}{2} \left[ \left( \frac{\partial \Phi}{\partial n} \right)^2 + \frac{\Phi_\xi^2}{r_\xi^2 + r^2 \theta_\xi^2} \right] + 2P_{\text{St}} - P_G - 2H. \quad (21)$$

In the above equation

$$\frac{D\Phi}{Dt} = \frac{\partial \Phi}{\partial t} + u \cdot \nabla \Phi = \frac{\partial \Phi}{\partial t} + |u|^2, \quad (22)$$

while  $\xi$  is a Lagrangian coordinate that identifies particles on the interface and is related to the arc length,  $s$ , of the interface by

$$\frac{\partial s}{\partial \xi} = (r_\xi^2 + r^2 \theta_\xi^2)^{1/2}, \quad 0 \leq \xi \leq 1; \quad (23)$$

$\xi$  as a subscript denotes partial differentiation. It should be pointed out that, in the context of Lagrangian formulation, both the scalar and the vector velocity potentials,  $\Phi$  and  $A$ , as well as the  $r$  and  $\theta$  coordinates of Lagrangian particles on the interface will be functions of  $\xi$ . Then, the mean curvature  $H$  is given by

$$-2H = \frac{1}{r^2 \theta_\xi \sin \theta} \left\{ \frac{\sin \theta (2r^2 \theta_\xi^2 + r_\xi^2)}{(r^2 \theta_\xi^2 + r_\xi^2)^{1/2}} - \frac{\partial}{\partial \xi} \left[ \frac{r r_\xi \sin \theta}{(r^2 \theta_\xi^2 + r_\xi^2)^{1/2}} \right] \right\}. \quad (24)$$

Owing to axisymmetry the derivatives with respect to  $\xi$  should satisfy the following conditions:

$$\frac{\partial r}{\partial \xi} = \frac{\partial \Phi}{\partial \xi} = \frac{\partial^2 \Phi}{\partial \xi \partial n} = \frac{\partial^2 \theta}{\partial \xi^2} = 0, \quad \text{at } \xi = 0, 1, \quad (25)$$

corresponding to the two poles of the coordinate system.

Following a standard procedure in the boundary integral literature, we recast the Laplacian in an integral form involving quantities evaluated at the interface, i.e., we introduce the boundary integral formulation of the Laplacian:

$$\begin{aligned} \Phi(\hat{r}, \hat{\theta}, t) + \int_0^1 [\Phi(r, \theta, t) - \Phi(\hat{r}, \hat{\theta}, t)] \\ \times \frac{\partial G}{\partial n}(\hat{r}, \hat{\theta}, r, \theta) r \sin \theta (r_\xi^2 + r^2 \theta_\xi^2)^{1/2} d\xi \\ = \int_0^1 \frac{\partial \Phi}{\partial n}(r, \theta, t) G(\hat{r}, \hat{\theta}, r, \theta) r \sin \theta (r_\xi^2 + r^2 \theta_\xi^2)^{1/2} d\xi, \end{aligned} \quad (26)$$

where hatted coordinates,  $\hat{r}, \hat{\theta}$ , depend on the location of the field point  $\hat{\xi}$  and are not subject to integration. The above equation relates the scalar velocity potential to its normal derivative at the interface and can be obtained by applying Green's third identity on the Laplacian and allowing the field point, where the potential is evaluated, to approach the interface.  $G$  and  $\partial G / \partial n$  denote the axisymmetric free space singular kernel of the Laplacian and its normal derivative, respectively.

### B. Weak viscous effects ( $\text{Oh} \ll 1$ )

When  $\text{Oh}$  is small the rotational part of the velocity field forms a boundary layer near the bubble's surface, where dissipation and inertia balance each other, so that the boundary condition of zero shear rate is satisfied at the interface. In order to capture this effect we introduce a new orthogonal coordinate system based on the arc-length  $s$  and azimuthal angle  $\varphi$ , as they are defined on the instantaneous position of the interface, and the distance,  $n$ , along the normal direction on any point in the interface. In this triply orthogonal coordinate system consisting of a Lamé group of surfaces based on the shape of the interface we know<sup>10</sup> that the metric along

the normal direction is  $h_n=1$  whereas those in the other two directions are  $h_t=1+O(n)$ ,  $h_\phi=r \sin \theta+O(n)$ , for an axisymmetric shape. Consequently, within a boundary layer, where  $n$  is small, the metrics are everywhere the same with those evaluated on the interface. For the same reason, the two unit vectors that are tangent to the family of surfaces parallel to the interface, and whose direction varies along the normal to the interface, within the boundary layer will be, roughly, identical to those defined on the interface. Thus, the gradient operator is defined in the boundary layer as

$$\nabla = \nabla_s + n \frac{\partial}{\partial n} + O(n) \approx t \frac{\partial}{\partial s} + \frac{e_\phi}{r \sin \theta} \frac{\partial}{\partial \phi} + n \frac{\partial}{\partial n}, \quad (27)$$

where  $\nabla_s$  is the surface gradient defined on the bubble's interface,  $t$  is the unit vector tangent along the generating curve of the axisymmetric interface and  $r$ ,  $\theta$ , are the coordinates that determine the instantaneous shape of the interface. The approximate expression for the gradient operator becomes exact when applied on the interface.

Next, following Lundgren and Mansour<sup>8</sup> we introduce the decomposition of the velocity and pressure fields in the problem formulation and integrate the equations of motion across the boundary layer. Upon introduction of the vector potential and the viscous correction of the pressure and considering that they vanish in the far field, we obtain equations that govern their variation on the bubble's surface:

$$U_t = -\frac{\partial A}{\partial n}, \quad U_n = \frac{1}{r \sin \theta} \frac{\partial}{\partial s}(r \sin \theta A), \quad (28)$$

$$\frac{DA}{Dt} = A(n \cdot \nabla u \cdot n - t \cdot \nabla u \cdot t) - \text{Oh} \frac{\partial U_t}{\partial n}, \quad (29)$$

$$p = A(t \cdot \nabla u \cdot n). \quad (30)$$

The last two equations are only valid on the bubble's interface. It should also be mentioned that their derivation entails boundary layer type arguments, with the thickness of the boundary layer,  $\delta$ , scaling like  $\delta \sim \text{Oh}^{1/2}$ , while  $U_t \sim \delta$ ,  $U_n \sim \delta^2$ ,  $p \sim \delta^2$  and  $A \sim \delta^2$ . Finally, we introduce the irrotational normal force balance, Eq. (22), in Eq. (12) to get the corrected expression for the evolution of the scalar velocity potential including weak viscous effects

$$\frac{D\Phi}{Dt} = \frac{u^2}{2} + 2P_\infty - 2P_G + 2p - 2H - 2\text{Oh}(n \cdot \nabla u \cdot n). \quad (31)$$

Since this approach was first introduced<sup>8</sup> it has been used ever since by other investigators as well, most notably Boulton-Stone and Blake.<sup>11</sup>

Before we summarize the equations that we solve in order to capture the dynamic behavior of the bubble, we have to stress that we work with variables that are evaluated on the surface and that can be calculated by solving the interfacial equations presented above. However, the tangential component of the vortical part of the velocity field, is given via the normal derivative of the vector potential, Eq. (28), which cannot be obtained by solving a differential equation defined solely on the interface. Consequently, since the location of a

free surface is determined purely by its normal velocity, with the tangential component operating as a mapping function that controls the relative position of the Lagrangian particles on the free surface, we move the particles in the following fashion:

$$\frac{dr_s}{dt} = u + U_n n. \quad (32)$$

As a result, instead of material points we refer to marker points that move according to the above expression without any loss in accuracy as far as the bubble shape is concerned. In terms of spherical coordinates, through which we describe the position of the particles, we have

$$\frac{dr}{dt} = \frac{(u_n + U_n)r\theta_s + u_t r_s}{\sqrt{r_s^2 + r^2\theta_s^2}}, \quad (33a)$$

$$\frac{d\theta}{dt} = \frac{u_t r\theta_s - (u_n + U_n)r_s}{r\sqrt{r_s^2 + r^2\theta_s^2}}, \quad (33b)$$

where subscript  $s$  denotes partial differentiation with respect to the arc-length  $s$  of the generating curve of the axisymmetric interface and  $d/dt = \partial/\partial t + (u + U_n n) \cdot \nabla$ . In the same fashion and in order to move the particles in a consistent manner, the equations describing the evolution of the scalar and vector potential become

$$\begin{aligned} \frac{d\Phi}{dt} &= \frac{u^2}{2} + u_n U_n + 2P_\infty - 2P_G + 2A(t \cdot \nabla u \cdot n) - 2H \\ &\quad - 2\text{Oh}(n \cdot \nabla u \cdot n), \end{aligned} \quad (34)$$

$$\frac{dA}{dt} = A(n \cdot \nabla u \cdot n - t \cdot \nabla u \cdot t) - \text{Oh} \frac{\partial U_t}{\partial n}. \quad (35)$$

In the last equation the additional term  $U_n(\partial A/\partial n)$  has been dropped from the right hand side as it is of higher order,  $O(\delta^3)$ . Overall, Eqs. (33a), (33b), (34), and (35), along with the integral equation (26), Eq. (14) that prescribes the variation of the pressure inside the bubble, the boundary conditions due to axisymmetry, i.e., Eq. (25) with the additional condition of vanishing vector potential at the poles,  $A(0, t) = A(\pi, t) = 0$ , and the initial conditions (1), (2), (7), and (8) provide the complete formulation of the dynamic behavior of the bubble. All the variables that are involved are evaluated on the surface, which, in view of the axisymmetry, renders the problem one-dimensional.

### C. Energy variation

Starting from the identity

$$\iiint_V \frac{\partial \Phi}{\partial t} \nabla^2 \Phi dV = 0, \quad (36)$$

and performing integration by parts we obtain

$$\oint \int_A \frac{\partial \Phi}{\partial t} \frac{\partial \Phi}{\partial n} dA - \frac{1}{2} \iiint_V \frac{\partial}{\partial t} [(\nabla \Phi)^2] dV = 0. \quad (37)$$

Invoking the Reynolds transport theorem we get

$$\begin{aligned} \frac{1}{2} \frac{d}{dt} \int \int \int_V [(\nabla\Phi)^2] dV &= \oint \int_A \frac{\partial\Phi}{\partial t} \frac{\partial\Phi}{\partial n} dA \\ &+ \frac{1}{2} \oint \int_A (\nabla\Phi)^2 (u_n + U_n) dA. \end{aligned} \quad (38)$$

Finally, integration by parts on the left-hand side integral and introduction of the dynamic boundary condition (34) provides the energy balance for the dynamics of the bubble

$$\begin{aligned} \frac{1}{2} \frac{d}{dt} \int \int_A \Phi \frac{\partial\Phi}{\partial n} dA - \frac{1}{2} \int \int_A u^2 U_n dA \\ + \int \int_A \frac{\partial\Phi}{\partial n} (2H + 2P_G - 2P_{St}) dA \\ = \int \int_A 2p \frac{\partial\Phi}{\partial n} dA - 2\text{Oh} \int \int_A \frac{\partial\Phi}{\partial n} \frac{\partial u_n}{\partial n} dA. \end{aligned} \quad (39)$$

The first two integrals on the left-hand side signify variations in the total kinetic energy of the system including the effect of the vortical velocity field. The first integral on the right-hand side represents energy loss due to the rotational part of the pressure whereas the second integral represents classical dissipation due to vorticity near a zero shear surface. The last term in Eq. (39) is equivalent to the expression given by Lamb,<sup>12</sup> for a moving surface at large  $\text{Re} = \text{Oh}^{-1}$ , involving the terms  $-\mu(dq'^2/dn)$  and  $2\mu n \cdot (u' \times \omega')$  in the integrand; in Lamb's notation  $q'$  is the magnitude of the velocity at the interface and  $\omega'$  is the vorticity. In the limit as  $\text{Oh}^{-1}$  tends to infinity the energy balance for inviscid<sup>7</sup> bubble oscillations is recovered,

$$\frac{d}{dt} \left[ \frac{1}{2} \oint \int_A \Phi \frac{\partial\Phi}{\partial n} dA + \oint \int_A dA + V \left( P_G + \frac{2P_{St}}{\gamma - 1} \right) \right] = 0. \quad (40)$$

### III. NUMERICAL SOLUTION

The numerical solution of the equation set presented at the end of Sec. II B is obtained in a fashion similar to the one presented by Pelekasis and Tsamopoulos<sup>7</sup> for the case of two interacting bubbles. More specifically, the boundary integral formulation was used in the Eulerian frame of reference, in order to establish a connection between the scalar potential and its normal derivative at the interface, whereas the Lagrangian representation was adopted for the motion of surface marker points in order to capture the evolution with time of the scalar and vector potentials. This requires solution of partial differential equations involving time and only one spatial dimension, as a combined result of axisymmetry and the use of boundary integral formulation. To this end, the azimuthal dependence has been integrated out of Eq. (26) thus leaving an integral equation of the first kind for the normal derivative of the scalar potential, given the potential, defined along the generating curve of the bubble's surface. Since the early studies in modeling cavitating bubbles<sup>13</sup> next to a solid or a free surface the boundary integral method has

extensively been used for capturing bubble oscillations, collapse or breakup.<sup>14-16</sup> For a review article on the boundary integral method for potential flow problems and comparative studies on the efficiency of different boundary integral formulations the interested reader is referred elsewhere.<sup>17-19</sup>

Despite the fact that reliable solvers of the full Navier-Stokes equations have also been developed the boundary integral method is still widely applied due to its superiority in capturing details of severely deformed interfaces, with large accuracy and minimum computational effort. The weak viscous correction of the boundary integral method, such as the one employed here, extends the validity of the standard potential theory formulation, to the extent that large displacement thickness effects are not present. This would be the case, for example, in situations with massive flow separation where the wake structure plays a central role in the dynamics, in which case resorting to the full Navier-Stokes becomes necessary. In the present study the appearance of liquid jets moving along the direction of elongation might entail such phenomena, but they occupy very thin regions and evolve very abruptly for any significant displacement thickness effect to alter the dynamic behavior captured by our numerical solution.

The fourth order explicit Runge-Kutta time integration scheme was employed due to its better stability characteristics.<sup>18</sup> In fact, it was seen that, for small initial deformations, doubling the number of elements along the interface required, roughly, a four times smaller time step for numerical stability. Solution of the unknowns of the problem is done sequentially. Once the complete state of the bubble is known at a certain time instant the surface marker points are moved in the manner prescribed by Eqs. (33a) and (33b) and their new coordinates are obtained. The updated values of the two potential functions are obtained in the same way. Next, using the boundary integral equation (26) we get the normal derivative of the scalar potential. Finally the bubble volume is calculated, the interior pressure is advanced, and the procedure is repeated until the bubble either breaks up or eventually returns to its equilibrium spherical shape. We are particularly interested in the dynamics of collapse or breakup. As explained in the following, mesh regridding takes place as time advances in order to prevent concentration of the marker points in certain regions of the interface leaving the rest of the interface misrepresented. Subsequently, the time step is adapted so that numerical stability is preserved.

Owing to the initial elongation and subsequent surface deformation, marker points are distributed in such a way as to prohibit large discrepancies in the element length while providing accurate discretization in regions of large curvature. This is accomplished by positioning the marker points along the interface so that the integral<sup>20</sup>

$$\int_0^1 (1 + d|-2H|)(r_\xi^2 + r^2 \theta_\xi^2) d\xi \quad (41)$$

is minimized;  $d$  is a parameter controlling the concentration of grid points in regions of high curvature. It ranges from  $10^{-2}$  to  $10^{-3}$  as the number of elements increases from 80 to 160. Decreasing  $d$  amounts to reducing the emphasis placed

upon curvature variations while regriding. As a result of this procedure the time step has to be adapted in order to maintain stability of the numerical scheme and properly resolve the capillary waves that arise as part of the dynamics of bubble deformation.

Initially, the dynamics is characterized by the high curvature regions around the two poles where the dimensionless radius of curvature is the smallest. Balancing the dynamic pressure with surface tension forces provides the proper time scale in this region as

$$\tau = \left( \frac{\rho R_0^3}{\sigma} \right)^{1/2}, \quad (42)$$

where  $R_0$  is the radius of curvature at the two elongated tips of the bubble. Consequently, in order to capture the dynamics in the early stages of the motion as parameter  $S$  decreases, since the minimum element size  $\Delta s_{\min}$  decreases with regriding, the time scale should also be decreased following the  $3/2$  power law mentioned above,  $\Delta t \sim (\Delta s_{\min})^{3/2}$ . This universal scaling law was also obtained elsewhere<sup>6</sup> in the context of capillary pinch-off of drops. In the present study the effect of initial elongation has to be accounted for as well. In practice, in order to respect the stability requirements of the Runge-Kutta time integrator which were found elsewhere<sup>18</sup> to obey a quadratic law,  $\Delta t \sim \Delta s_{\min}^2$ , and to account for the decreasing radius of curvature as parameter  $S$  decreases, in the simulations to be presented hereafter the time step was initially set to  $\Delta t = \Delta s_{\min}^2 S$ . This scaling was found to be appropriate in the beginning of the bubble motion. Once the simulation commences, for a given value of  $S$ , the time step is adapted according to the following law:

$$\frac{\Delta t^{\text{new}}}{\Delta t^{\text{old}}} = \left( \frac{\Delta s_{\min}^{\text{new}}}{\Delta s_{\min}^{\text{old}}} \right)^\alpha \frac{H_{\min}^{\text{new}}}{H_{\min}^{\text{old}}}, \quad (43)$$

where  $H_{\min}$  is the minimum mean radius of curvature on the bubble's surface and  $\alpha$  an adjustable parameter that is initially set to one. As time evolves, the time step has to be further reduced due to the appearance of two high-speed jets approaching each other along the axis of symmetry, hence parameter  $\alpha$  has to be increased accordingly. During collapse areas with very small radius of curvature appear in the form of dimples that eventually touch at the equatorial plain. Accurate resolution of such areas requires further remeshing and time step adaptation, which is performed by further increasing  $\alpha$  which had to become as large as 3 and 4. More specifically, in the beginning of the simulation the time step was in the order of  $10^{-5}$  whereas during collapse it had to be dropped to  $10^{-8}$ .

It should also be stressed that, for calculations with finite Oh, marker points are used for tracking the evolution of the interface instead of Lagrangian particles. This is a result of our inability to evaluate the tangential component of the vortical velocity field solely based on quantities that are defined on the boundary. Nevertheless, this does not restrict the validity of our results since the shape of a free surface can always be found from information regarding the normal component of the velocity of particles residing on the interface. The tangential component simply acts as a function that

maps points between the previous and the current location of the interface. This is a well-known result that has been used by previous investigators<sup>21</sup> in order to optimize the distribution of the grid points on the interface and avoid grid distortion. In the present study the potential part of the tangential component of the velocity of surface particles is used for updating the position of the interface, along with the normal component of the potential and vortical parts, without any compromise in numerical accuracy.

Numerical calculation of the azimuthal component of the vector potential, involves interpolation of second order derivatives of the scalar potential in a manner that is not amenable to reduction of order via integration by parts. Consequently, as the simulation proceeds, short wave instabilities tend to appear whose wavelength is on the order of minimum element size. Such short wave instabilities often appear in high Oh<sup>-1</sup> calculations<sup>8,18</sup> and cannot be eliminated by mesh refinement alone. The standard procedure in order to circumvent this problem is to implement filtering of the higher modes while monitoring the energy of the system so that it is dissipated appropriately. Inviscid calculations do not exhibit such instabilities hence filtering is avoided. However, in all the simulations to be presented in the following where Oh is taken to be small but finite, after a certain number of time steps the vector potential is filtered by introducing the fourth order derivative with respect to  $\xi$ ,

$$\frac{\partial A}{\partial t} = \lambda \frac{\partial^4 A}{\partial \xi^4}. \quad (44)$$

The above equation is discretized with the second order accurate fully implicit scheme,

$$A'_j = A_j + \frac{\lambda \Delta t}{\Delta \xi^4} (A'_{j+2} - 4A'_{j+1} + 6A'_j - 4A'_{j-1} + A'_{j-2}), \quad (45)$$

which possesses improved stability characteristics;  $\lambda \Delta t / \Delta \xi^4$  was set to a large value, typically between 100 and 1000, for stability reasons. As will be seen in the numerical tests presented in the end of this section, this methodology allows for accurate and efficient evaluation of the vortical part of the flow, which is essential for handling weak viscous effects.

Another important aspect of the numerical methodology that is employed here has to do with the use of symmetry with respect to the equatorial plane in order to reduce the storage requirements and processing time for a given level of accuracy. When the shape of the bubble is expected to remain symmetric throughout the simulation, the domain of discretization can be halved so that it includes only one of the two hemispheres, say the north. Consequently and in view of axisymmetry, only half of the generating curve that connects the north and the south pole needs to be discretized and the size of the full matrix, that has to be constructed and inverted for the calculation of the normal derivative of the scalar potential, becomes four times smaller which constitutes a significant reduction in the computational load. To this end, the same symmetry boundary conditions that were originally imposed at the south pole, Eq. (25), are now implemented at the equator where coordinate  $\xi'$  is set to one in the new formulation. In addition, integral equation (26) is

rearranged to incorporate symmetry. More specifically, the single layer kernel,  $G$ , is symmetric when the shape of the interface is symmetric with respect to the equator and consequently the integral containing kernel  $G$  in Eq. (26) becomes

$$\begin{aligned} & \int_0^1 \frac{\partial \Phi}{\partial n}(r, \theta, t) G(\hat{r}, \hat{\theta}, r, \theta) r \sin \theta (r_\xi^2 + r^2 \theta_\xi^2)^{1/2} d\xi \\ &= 2 \int_0^1 \frac{\partial \Phi}{\partial n}(r, \theta, t) G(\hat{r}, \hat{\theta}, r, \theta) r \sin \theta (r_{\xi'}^2 + r^2 \theta_{\xi'}^2)^{1/2} d\xi', \end{aligned} \quad (46)$$

with  $r, \theta, \hat{r}, \hat{\theta}$ , defined along the line connecting the north pole with the equator. The double layer kernel on the other hand is not symmetric and as a result the integral containing  $\partial G / \partial n$  becomes

$$\begin{aligned} & \int_0^1 [\Phi(r, \theta, t) - \Phi(\hat{r}, \hat{\theta}, t)] \frac{\partial G}{\partial n}(\hat{r}, \hat{\theta}, r, \theta) r \sin \theta (r_\xi^2 + r^2 \theta_\xi^2)^{1/2} d\xi \\ &= \int_0^1 [\Phi(r, \theta, t) - \Phi(\hat{r}, \hat{\theta}, t)] \frac{\partial G}{\partial n}(\hat{r}, \hat{\theta}, r, \theta) \\ & \quad \times r \sin \theta (r_{\xi'}^2 + r^2 \theta_{\xi'}^2)^{1/2} d\xi' - \int_0^1 [\Phi(r, \omega, t) - \Phi(\hat{r}, \hat{\theta}, t)] \\ & \quad \times \frac{\partial G}{\partial n}(\hat{r}, \hat{\theta}, r, \omega + \pi/2) r \sin \omega (r_{\xi'}^2 + r^2 \omega_{\xi'}^2)^{1/2} d\xi', \end{aligned} \quad (47)$$

where

$$\omega = \theta - \pi/2 \leq \pi/2, \quad \Phi(r, \omega, t) = \Phi(r, \omega + \pi/2, t), \quad (48)$$

$$\frac{\partial \Phi}{\partial n}(r, \omega, t) = \frac{\partial \Phi}{\partial n}(r, \omega + \pi/2, t).$$

As the number of elements increases construction of the system matrix, which is full as is normally the case with the boundary integral methodology, the most time consuming part of the computation takes up more than 80% of the CPU time.<sup>7,18</sup> In order to optimize computational speed we resort to parallel strategies. In particular, the system matrix is constructed in a parallel fashion with different processors dedicated to different rows of the matrix. The algorithm is implemented on a LINUX Cluster with 4 Xeon processors with significant savings in processing time.

### Validation of the numerical scheme

The validity of the above numerical implementation was investigated in a number of cases some of which are presented in this section. First of all the linear prediction of the breathing mode frequency was recovered when the initial elongation was relatively small,  $S \sim 1$ . Figure 2 shows the time evolution of the first Legendre mode,  $P_0$ , that is associated with volume oscillations, and the second Legendre mode,  $P_2$ , for a slightly elongated bubble,  $S=0.8$ , of equilibrium radius  $R=5.8 \mu\text{m}$  that is oscillating in water at atmospheric pressure;  $P_{St}=4.1$ ,  $\varepsilon_B=0$ , water is taken to be inviscid and 100 elements are used for the discretization of the

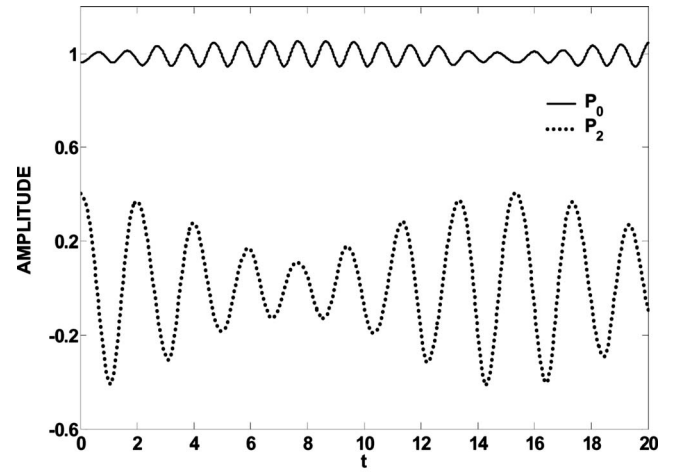


FIG. 2. Time evolution of the coefficients of Legendre modes  $P_0$  and  $P_2$  for the decomposition of the position of the interface  $f$ ;  $S=0.8$ ,  $P_{St}=4.1$ ,  $\text{Oh} \rightarrow 0$ ,  $\varepsilon_B=0$ , with 100 elements in the region  $0 \leq \theta \leq \pi$ .

interface. Despite the moderate value of  $\varepsilon$  orthogonal decomposition of the shape in the Legendre eigenmodes reveals that  $P_0$  and  $P_2$  dominate and oscillate at a frequency that is slightly smaller than that predicted by linear theory,

$$\omega_0 = [6(P_{St} + 1)\gamma - 2]^{1/2}, \quad \omega_k = [(k^2 - 1)(k + 2)]^{1/2}, \quad (49)$$

$$k \geq 1,$$

as a result of inertia. At a slower time scale there is an exchange of energy between the two modes that is manifested in the beat exhibited in the oscillations of  $P_0$  and  $P_2$  in Fig. 2. Physically this reflects the inward motion of the bubble along its two poles, as a result of the increased curvature in that region, which tends to restore its spherical shape at equilibrium. Subsequently, this motion is reversed due to the compressibility of the bubble and the whole cycle is repeated. The total energy remains constant, as expected in the absence of any damping mechanism, at the value predicted by integrating the governing equations over the entire flow domain, Eq. (40).

The effect of viscosity was also investigated by imposing a sinusoidal disturbance, of the type described by Eq. (2), on the static pressure in the far field. The forcing frequency is set to the dimensionless fundamental frequency of  $P_2$ ,  $\omega_f = \omega_2$ ,  $S$  to 1 and  $\varepsilon$  to 0.5.  $\text{Oh}^{-1}$  was set to the value corresponding to a bubble with equilibrium radius  $R=5.8 \mu\text{m}$ , i.e.,  $\text{Oh}^{-1}=20.5$ . Weak viscous analysis may not be exactly valid at this relatively low value, however it does provide us with a reliable estimate of viscous dissipation. In any case, this particular simulation was intended to serve as a test case for the behavior of the numerical scheme employed for calculating the vector potential and for establishing the validity of the filtering scheme. The bubble is initially performing pure volume oscillations but eventually acquires a periodically deformed shape with  $P_0$  and  $P_2$  as the only eigenmodes and  $\omega_2$  as the corresponding frequency, Fig. 3.

Finally, our numerical methodology was validated against mesh refinement for a rather demanding flow situation. Namely, the case with  $S=0.6$  and  $\text{Oh}^{-1}=1000$  was in-

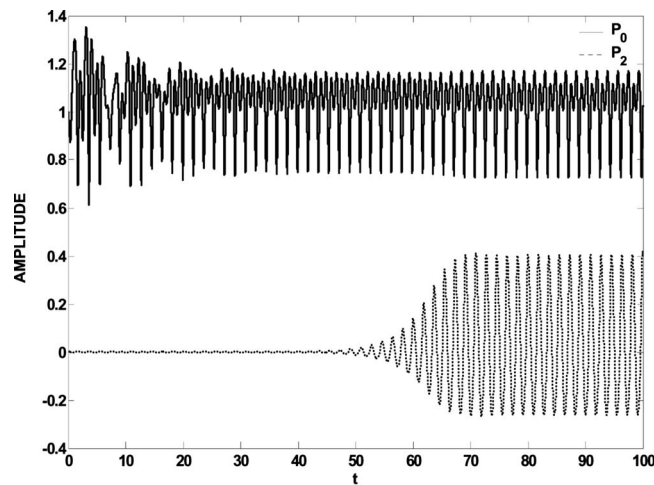


FIG. 3. Time evolution of the coefficients of Legendre modes  $P_0$  and  $P_2$  for the decomposition of the position of the interface  $f$ ;  $S=1.0$ ,  $P_{St}=4.1$ ,  $\varepsilon=0.5$ ,  $\omega_f=\omega_2=3.46$ ,  $Oh^{-1}=20.5$ , with 100 elements in the region  $0 \leq \theta \leq \pi$ .

investigated and the evolution of the bubble shape and total energy was obtained from the initial stages of bubble motion until collapse, with 75 and 100 elements along half of the generating curve connecting the two poles in view of the symmetry of the shape, Figs. 4(a) and 4(c). The initial inward motion of the bubble along its axis of symmetry, as a result of the reduced curvature at the two poles, is accurately captured and, more importantly, the final stages of collapse are obtained with the formation of what seems to be two countercurrent liquid jets, Fig. 4(b), that eventually meet at the equatorial plane. Dimple formation at the rounded ends of the two jets is clearly exhibited by the corresponding shapes, along with the formation of a small satellite bubble after collapse, Fig. 4(c). More details on the physics of collapse are presented in the next section. The variation of the total energy of the system is also monitored, Fig. 5, as an additional means to check the validity of the numerical treatment of viscous effects. The time derivative of the kinetic and potential energy of the bubble is calculated numerically and compared against dissipation, in the manner shown in Eq. (39), with more than satisfactory agreement at least for the range of the calculation over which the kinetic energy does not change very abruptly. In the latter case numerical differentiation of the total kinetic energy becomes less accurate and monitoring of Eq. (39) quite difficult. From this stage on we have to resort to mesh refinement for establishing the validity of the numerical solution.

#### IV. RESULTS AND DISCUSSION

Based on the asymptotic analysis and the numerical methodology that were presented in the previous sections, a series of simulations was carried out in an effort to capture the initial dynamics as well as the final stages of collapse, whenever that was indeed the case, for small or large initial elongations. Inviscid oscillations as well as weak viscous effects were also accounted for by adjusting  $Oh$ . Finally the effects of small internal overpressure and initial fore-aft asymmetry in the bubble shape were included.

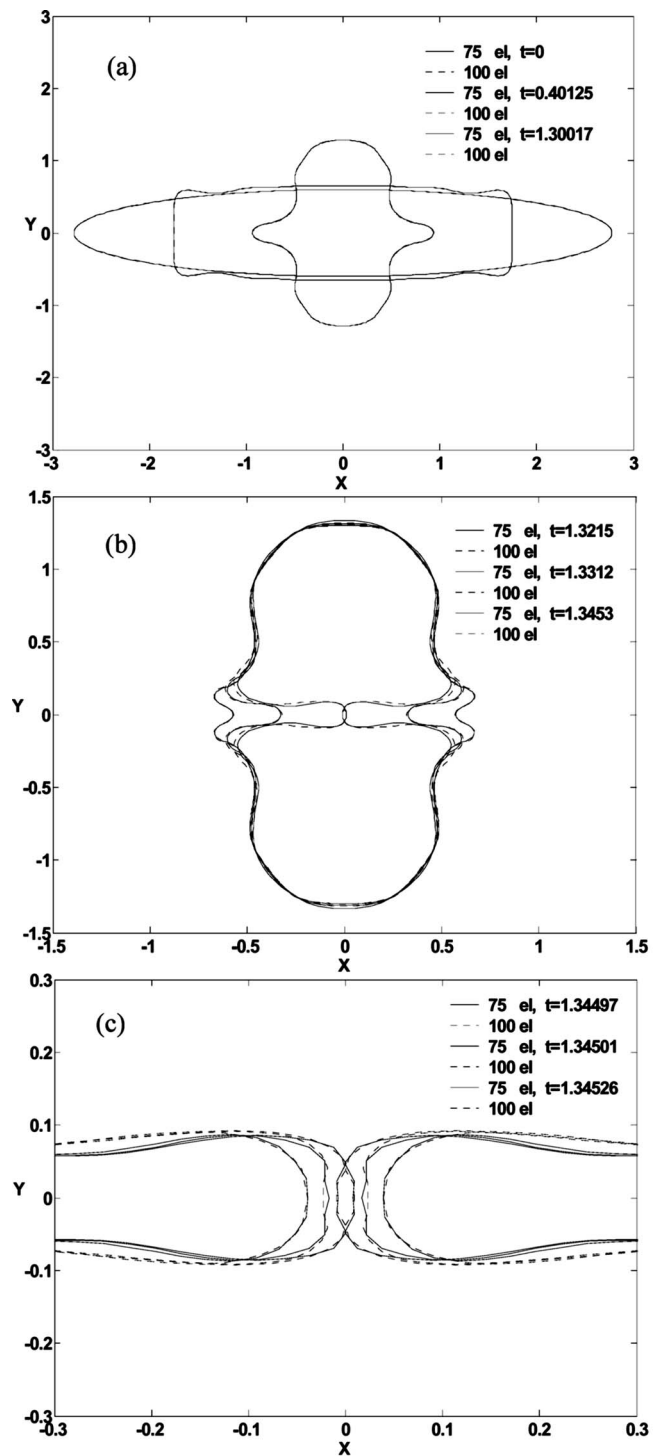


FIG. 4. Time evolution of the shape of the bubble (a) in the beginning of the motion, (b) during jet formation, and (c) during collapse;  $S=0.6$ ,  $P_{St}=4.1$ ,  $Oh^{-1}=1000$ , with 75 and 100 elements in the region  $0 \leq \theta \leq \pi/2$ .

In this fashion it was found that, for small or moderate initial elongations,  $S > 0.6$ , of micrometer-size bubbles,  $R = 5.8 \mu\text{m}$ , oscillating in water at atmospheric pressure,  $P_{St} = 4.1$ , and no internal overpressure,  $\varepsilon_B = 0$ , the dynamics is initially determined by the energy exchange between volume oscillations, dominated by  $P_0$ , and shape oscillations, dominated by  $P_2$ . This tendency is clearly exhibited in Fig. 2, where the evolution of the corresponding modes is plotted vs

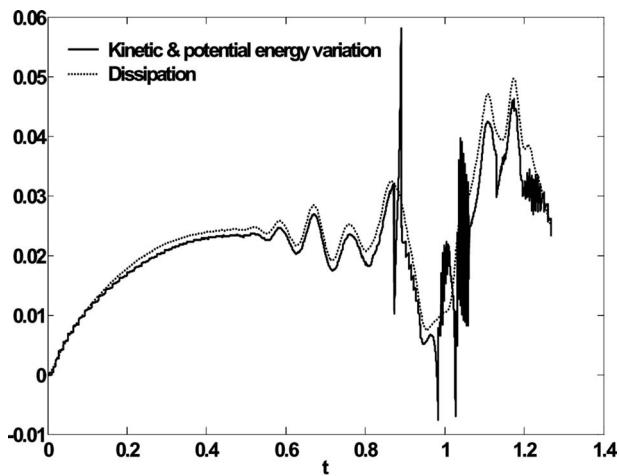


FIG. 5. Comparison between time variation of the total kinetic and potential energy and dissipation;  $S=0.6$ ,  $P_{St}=4.1$ ,  $Oh^{-1}=1000$ , with 100 elements in the region  $0 \leq \theta \leq \pi/2$ .

time, as well as in Fig. 6, where the shape deformation of the bubble is followed for a number of periods of the breathing mode,  $T_0=2\pi/\omega_0$ , when  $S=0.8$  and viscous dissipation is neglected,  $Re \rightarrow \infty$ . In this case the bubble oscillates indefinitely, without breaking up, while its shape is deformed in a manner determined by slow energy transfer to higher modes. When viscous effects are included in the model the shape of the bubble eventually returns to its equilibrium spherically symmetric configuration, see Fig. 7 for the case with  $Oh^{-1}=500$ . This process occurs faster with decreasing  $Oh^{-1}$ . The slow “beat” between  $P_0$  and  $P_2$  with the final domination of  $P_0$ , as a result of viscous damping, is shown in Figs. 8(a) and 8(b) for  $P_0$  when  $Oh^{-1}=1000$  and 500 and in Figs. 8(c) and 8(d) for  $P_2$  and the same values of  $Oh^{-1}$ . The pattern was seen to persist for quite a wide range of initial deformations until when  $S=0.62$  and  $Oh \rightarrow 0$  the two opposite ends of the bubble touch each other at the equatorial plane. In this case

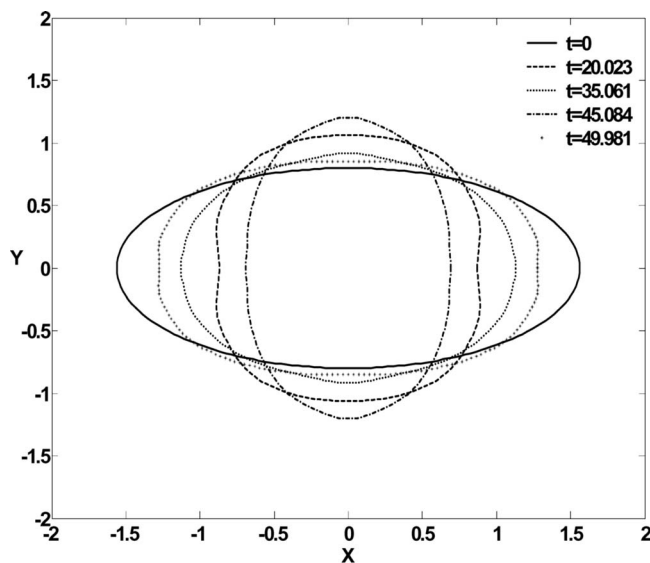


FIG. 6. Bubble shapes for the inviscid case with  $S=0.8$ ,  $\varepsilon_B=0$  and 50 elements in the region  $0 \leq \theta \leq \pi/2$ .

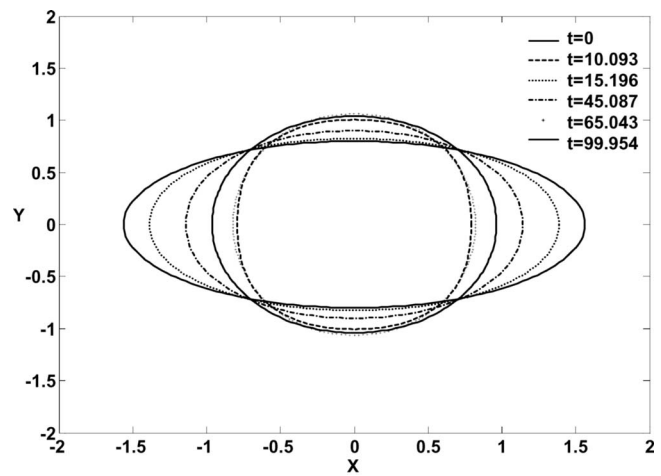


FIG. 7. Bubble shapes for the case with  $S=0.8$ ,  $\varepsilon_B=0$ ,  $Oh^{-1}=500$  and 50 elements in the region  $0 \leq \theta \leq \pi/2$ .

the kinetic energy that is acquired near the two poles of the bubble as they move towards each other due to the initial elongation, is just enough to overcome the reaction exercised by the gas inside the bubble, in the form of an increase in its interior pressure as a result of its compressibility. When viscous effects are included the bubble eventually settles to a sphere, as expected.

As the initial elongation further increases,  $S=0.6$ , this interesting dynamic effect is more pronounced towards the final stages of the bubble collapse. The initially prolate shaped bubble soon acquires an oblate form, as was the case with smaller initial deformations, except that now the two poles exhibit more intense deformations, the regions near them are dominated by higher harmonics, and consequently they undergo faster oscillations locally; see Fig. 9(a) when  $S=0.6$  and  $Oh^{-1} \rightarrow \infty$ . Eventually, two high-speed jets are formed at the two poles that approach each other along the axis of symmetry. As the two jets approach the equatorial plane they spread and form rounded ends that keep approaching, Fig. 9(b), until they eventually collide.

In the present study the film that is formed in the region between the two jet-tips that are approaching each other, exerts no lubrication force upon them owing to the negligible viscosity of the gas inside the bubble. Nevertheless, the two tips interact since they are part of the bubble’s interface. Formally, this is exemplified by the integral form of Laplace’s equation, which accounts for the interaction between different parts of the moving interface and how this reflects on the interfacial velocity. Thus, the tip of the two jets acquires a rounded shape due to its progressive deceleration as it approaches the equatorial plane, where the normal velocity vanishes if symmetry is to be respected. Since the tangential velocity is zero at the poles anyway, for axisymmetric shapes, a local pressure maximum is established there. Thus, fluid entering this region prefers to move in a direction other than that defined by the axis of symmetry. This signifies the formation of a pressure minimum off the axis of symmetry on the liquid side, which, given that the pressure is uniform inside the bubble, results in the appearance of a dimple with very high curvature on either side of

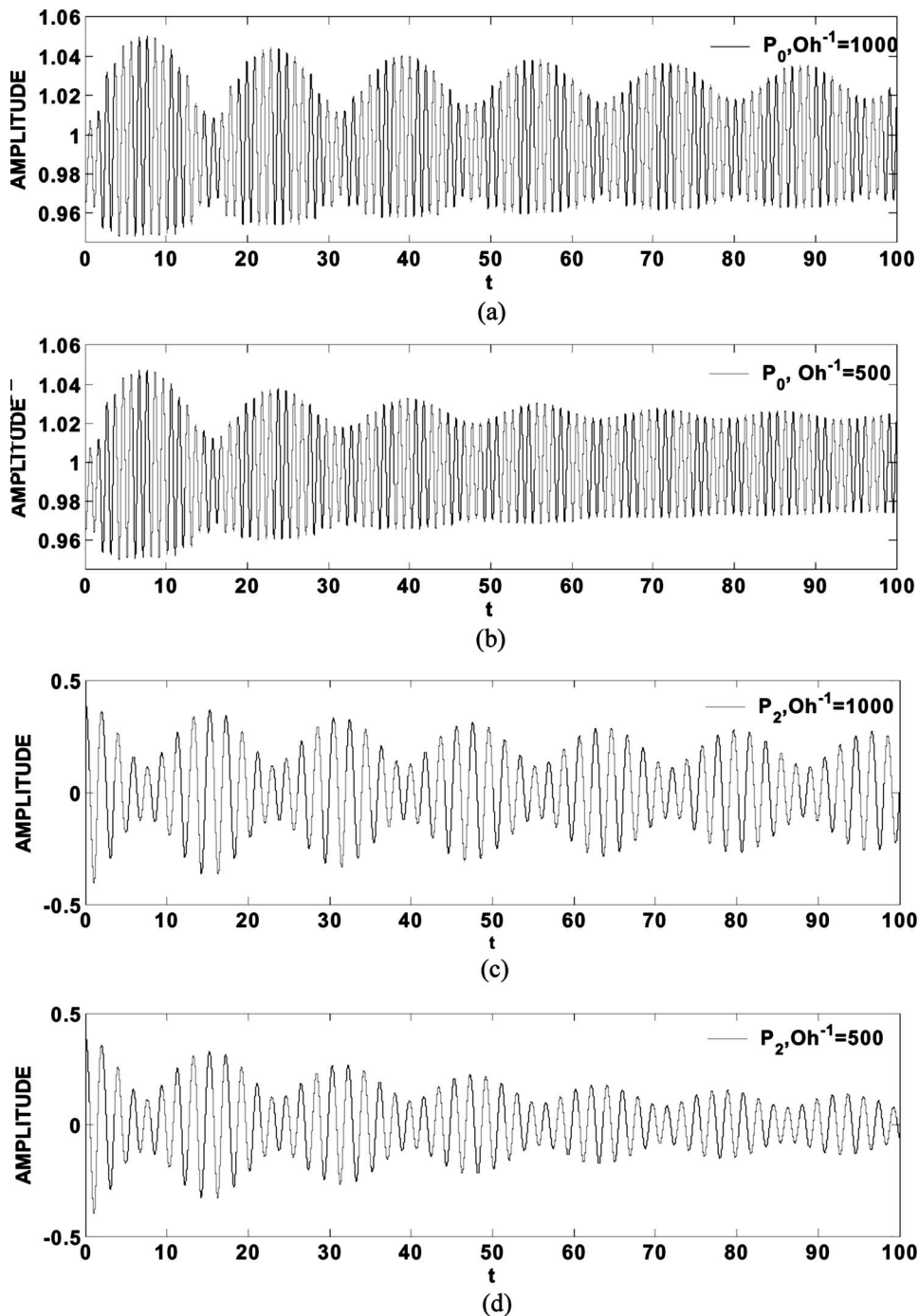


FIG. 8. Time evolution of the coefficients of Legendre modes: (a)  $P_0$ ,  $Oh^{-1}=1000$ , (b)  $P_0$ ,  $Oh^{-1}=500$ , (c)  $P_2$ ,  $Oh^{-1}=1000$  and (d)  $P_2$ ,  $Oh^{-1}=500$ , for the case with  $S=0.8$ ,  $\varepsilon_B=0$  and 50 elements in the region  $0 \leq \theta \leq \pi/2$ .

the axis of symmetry. In the present study pressure variations inside the bubble follow changes in the bubble's volume, which occurs on a much slower time scale than the growth and approach of the dimples that appear on the two jets. Finally, the dimples that form on either side of the equator upon the rounded ends of the two jets approach each other until they touch, Fig. 9(c), giving rise to a small satellite bubble, which occupies the region circumscribed by the dimples. The tiny satellite bubble is surrounded by the rest of the bubble which has now acquired a toroidal shape.

Dimple formation is an effect that is also observed whenever two Newtonian liquid drops approach each other, whether they are coated by surfactants or not. It should be

pointed out, however, that in the present study the minimum distance between the two rounded ends of the two jets eventually vanishes due to the absence of viscous stresses in the gas phase. In fact, final coalescence is also possible when two drops that are dispersed in another liquid are approaching each other, provided that normal viscous stresses and inertia effects are negligible<sup>22</sup> in the continuous phase.

An interesting aspect of the collapsing process of elongated bubbles concerns the existence of universalities in the period of time between dimple formation and the coalescence of the two jets when the dimples lying on opposite jets touch upon each other. This is a natural extension of previous studies<sup>5,6</sup> on the capillary pinch-off in inviscid liquids. In the

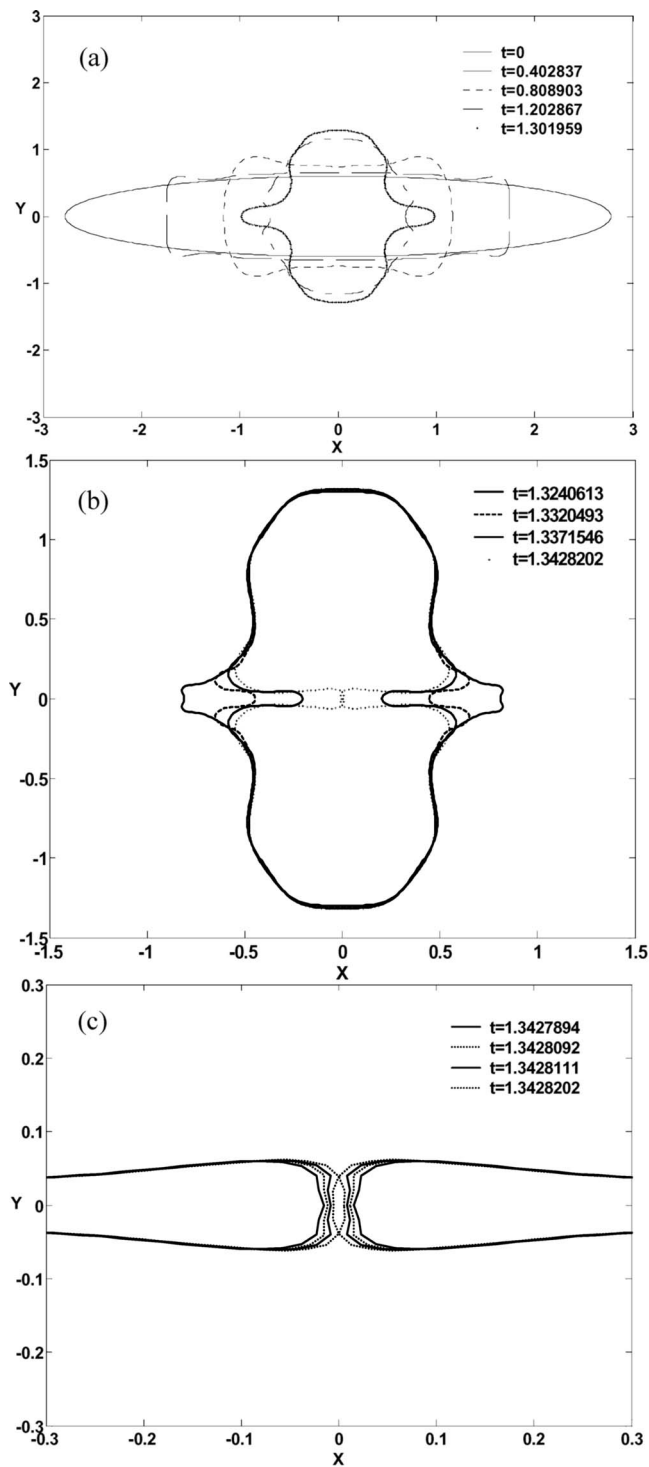


FIG. 9. Time evolution of the shape of the bubble (a) in the beginning of the motion, (b) during jet formation, and (c) during collapse;  $S=0.6$ ,  $P_{Si}=4.1$ , infinite  $Oh^{-1}$ , with 100 elements in the region  $0 \leq \theta \leq \pi/2$ .

latter studies it was shown that the process of capillary breakup in liquid drops or jets, excluding viscous effects, is governed by the balance between surface tension and dynamic pressure in the manner illustrated by Eq. (42). In this fashion, it was shown that the radius of curvature of each neck on the interface where pinch-off occurs as well as the minimum distance between the two necks in the pinching region eventually vanish and, more specifically, the time to

pinch-off scales with the  $3/2$  power of either one of the above quantities. In the present study we show that this indeed is the case with the distance,  $D$ , between two approaching dimples lying on opposite jets and the time for bubble collapse. As can be seen from the close-up on the collapsing process shown in Fig. 9(c), the dimples tend to become more acute as they approach, implying a vanishing radius of curvature as they touch, and the distance between them raised to the  $3/2$  scales linearly with the time to collapse, Fig. 10(a). This is a result that is supported by mesh refinement, with the element size in the region around the dimples remaining much smaller than the minimum distance between them.

In order to corroborate the breakup mechanism that was outlined above the inviscid case with  $S=0.62$  was recalculated starting from a point in time for which a well-rounded jet tip is formed. This is the parameter value for which the microbubble is formed for the first time in the central region of the original bubble. The solution vector obtained up to that time with 100 elements placed along the generating curve connecting the north pole and the equator, was interpolated with 150 elements to produce a more accurate description of the interfacial shape and velocity. The time step was adapted according to Eq. (43) and the solution was advanced in time until a collapse took place. As illustrated by a close-up on the details of the bubble motion shown in Fig. 11, the basic features of the shape of the interface near the equator are reproduced by the refined mesh and the dimples are captured more accurately, Figs. 11(a) and 11(b);  $\xi=1$  and 0 represent particles located at the equator and the north pole, respectively. The evolution of the overall bubble shape is not very different from that shown in Fig. 9, hence it is not shown. As time advances the dimples tend to become more acute in shape and tend to eventually touch following the scaling law that was discussed in the previous paragraph. As soon as the dimple is formed,  $t \approx 1.355$  from Fig. 11(b), the pressure on the liquid side acquires a minimum, Fig. 11(e), which explains the increased curvature in the same area. The normal velocity,  $\partial\Phi/\partial n'$  with  $n'$  pointing towards the liquid, in the vicinity of the dimple is negative indicating motion towards the equatorial plane, Fig. 11(c).

The persistence of the above pattern was investigated for varying  $Oh$  and initial elongation  $S$  and it was seen to indeed occur until a critical  $Oh^{-1}$ , below which the motion of the two jets is damped strongly enough to prevent them from getting too close and coalescing to form the smaller satellite and the larger toroidal bubbles. The lowest value of  $Oh^{-1}$  for which the above mode of collapse was observed for the case with  $S=0.6$ , was found to be  $Oh_{cr}^{-1} \sim 600$ . The sequence of bubble shapes as time elapses is shown in Figs. 4(a)–4(c) from the beginning of the deformation until collapse, for the case with  $Oh^{-1}=1000$ . As expected, the increasing effect of viscosity decelerates the two jets and causes them to spread, in comparison with the inviscid simulation, before they become rounded at the tips and eventually touch. If  $Oh^{-1}$  is further decreased to 400 the bubble eventually returns to its equilibrium spherically symmetric configuration, Fig. 12. Decreasing  $S$  to 0.55, which amounts to intensifying the initial elongation, results in two faster and narrower countercurrent jets. This is a result of the increased initial elongation that

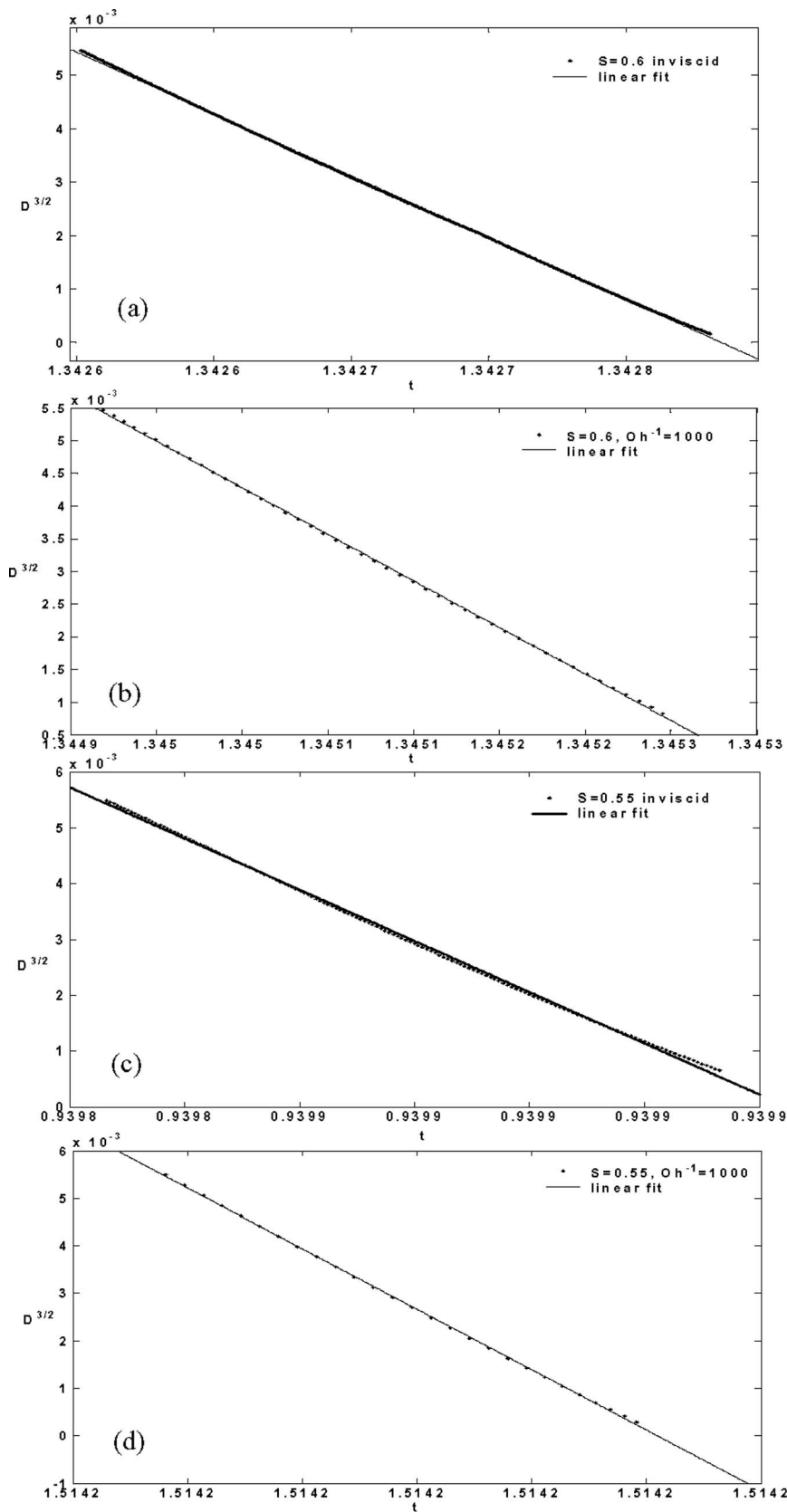


FIG. 10. Time evolution of the distance  $D$ , raised to the 3/2 power, between the dimples that are formed on countercurrent jets when  $\varepsilon_B=0$  and (a)  $S=0.6$ ,  $Oh^{-1}$  infinite, (b)  $S=0.6$ ,  $Oh^{-1}=1000$ , (c)  $S=0.55$ ,  $Oh^{-1}$  infinite and (d)  $S=0.55$ ,  $Oh^{-1}=1000$ ; 100 and 130 elements were used in the region  $0 \leq \theta \leq \pi/2$  for the cases with  $S=0.6$  and 0.55, respectively.

induces larger velocities in the vicinity of the two poles. The jets again form rounded ends as they approach each other until they eventually touch at the two protruding dimples, as illustrated in Figs. 13(a)–13(c) for the inviscid case. The final

stages of coalescence of the rounded ends of the two jets are governed by the scaling rule mentioned above, namely that the distance between opposite facing dimples, raised to the 3/2 power, scales linearly with the time to pinch-off, Fig.

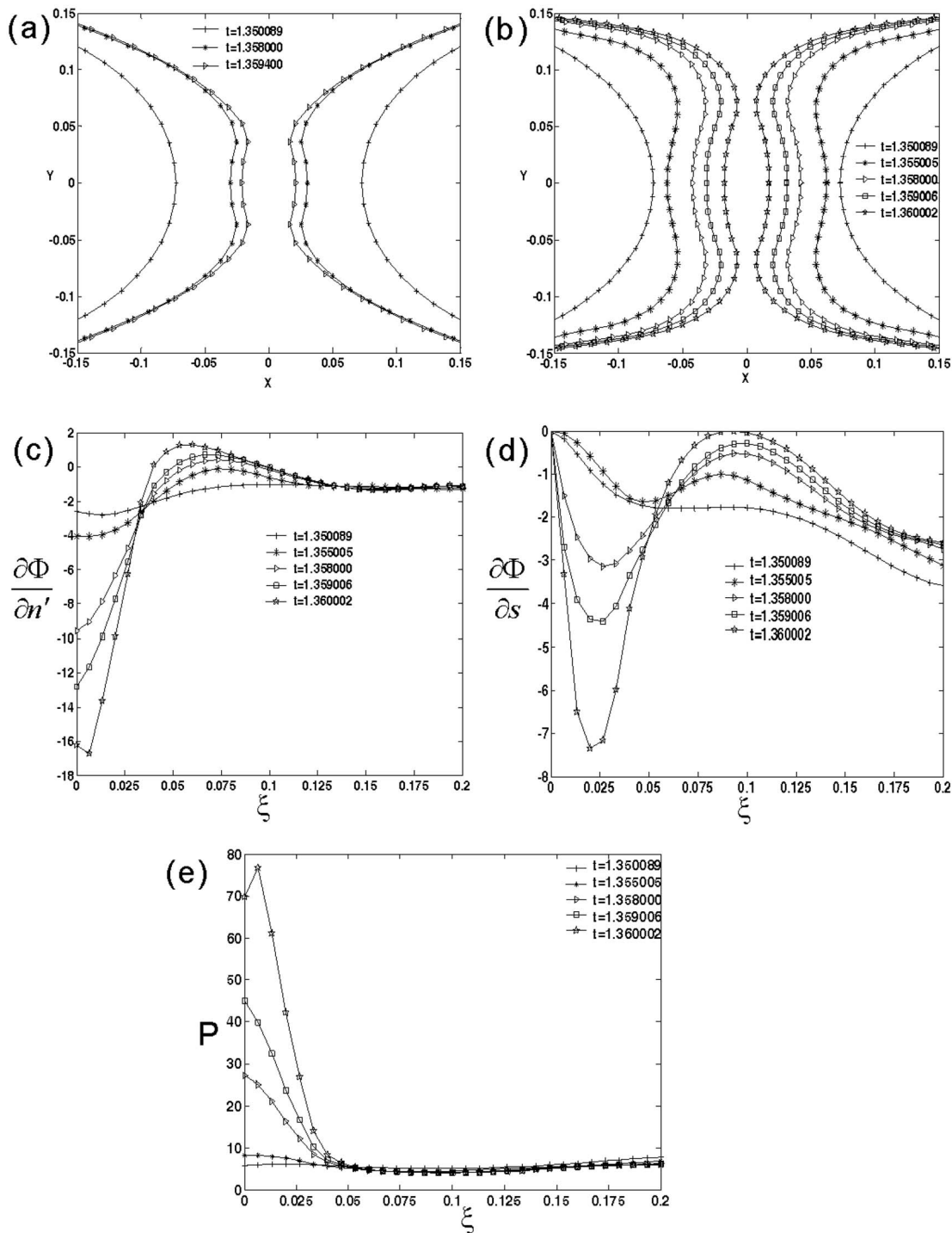


FIG. 11. Close-up on the solution vector in the vicinity of the dimple shortly before collapse when  $S=0.62$ ,  $\varepsilon_B=0$ ,  $Oh=0$ ; (a) shape of the interface with 100 elements in the region  $0 \leq \theta \leq \pi/2$  and (b) shape of the interface, (c) normal velocity, (d) tangential velocity and (e) liquid pressure with 150 elements in the region  $0 \leq \theta \leq \pi/2$ .

10(c). Again, this behavior persists until a threshold value of  $Oh^{-1} \sim 200$ . The evolution of deformed bubble shapes for the case with  $Oh^{-1} = 1000$  is illustrated in Figs. 14(a)–14(c), from initial elongation until collapse. In this case the two counter-current jets are thinner compared to the situation with  $S = 0.6$  and  $Oh^{-1} = 1000$  but thicker than the inviscid situation with  $S = 0.55$ , as expected due to the smaller initial elongation and negligible viscous dissipation, respectively. The results with finite  $Oh$  were examined with regards to the uni-

versal scaling law governing the collapsing process and it was seen that the latter is more or less true for large but finite values of  $Oh^{-1}$ . This is illustrated in Figs. 10(b) and 10(d), where the minimum distance between the counter-current jets, raised to the  $3/2$  power, is plotted against time from pinch-off for the cases with  $Oh^{-1} = 1000$  and  $S = 0.6$  and  $0.55$ , respectively. As mentioned above, this pattern ceases to exist below a threshold value of  $Oh^{-1}$  at which point the bubble returns to the spherical shape.

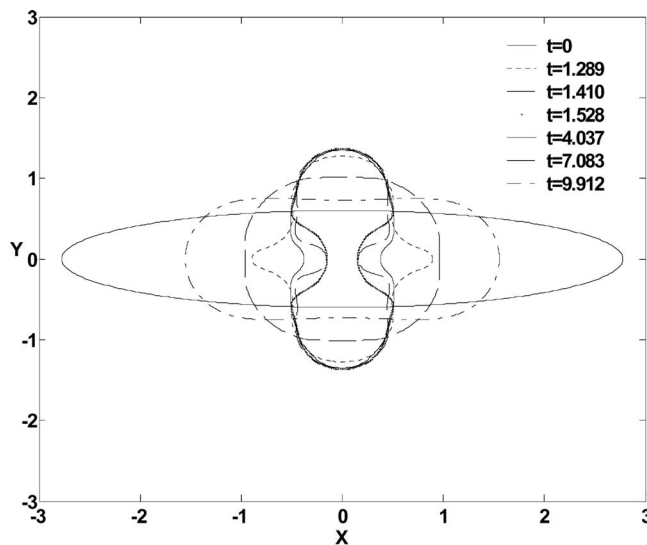


FIG. 12. Bubble shapes for the case with  $S=0.6$ ,  $\varepsilon_B=0$ ,  $Oh^{-1}=400$  and 100 elements in the region  $0 \leq \theta \leq \pi/2$ .

At this point it should be stressed that similar boundary integral studies on bubble breakup have been carried out by other investigators as well, in the presence of initial shape perturbations<sup>15</sup> and large initial overpressure,<sup>16</sup> but under less severe initial elongation, hence the more prominent role of jet formation in the breakup process that was identified in the present study in comparison with Ref. 16 where jet formation was also captured. It should also be pointed out that as  $S$  decreases even further the motion at the two poles becomes so fast that the time step required for capturing the initial deformation and collapse phases of the bubble motion becomes prohibitively small. Consequently, we refrained from reducing  $S$  below 0.55. Nevertheless, we anticipate that with increasing initial elongation the mode of collapse will change as different phenomena may emerge. For example, already for the case with  $S=0.55$  the tendency of the two jets to pinch-off before they coalesce is evident in Fig. 13(b) where a distinct neck formation is observed as a result of the fast speed of approach.

Another interesting aspect of the simulations is the size of the satellite bubble that is formed after coalescence of the two jets takes place. It is seen in Fig. 15(b) when  $Oh^{-1}=1000$  but also from Figs. 9(c) and 13(c) for the inviscid case, that the size of the satellite bubble decreases with decreasing  $S$ , evidently as a result of the decreasing thickness of the two penetrating jets and, consequently, of the decreasing radius of the ensuing rounded ends. As a matter of fact it was identified as a pattern in the present study that, as long as the above described collapse mode persisted, deceleration of the process of jet formation and subsequent reduction of jet velocity leads to larger sizes of the satellite bubble. Indeed reduction of  $Oh^{-1}$  leads to larger bubble sizes, see Fig. 15(b), for the case with  $S=0.6$  and Figs. 14(c) and 13(c) for the case with  $S=0.55$ . In fact, so does increasing the internal overpressure,  $\varepsilon_B$ . In this case the speed by which the elongated bubble retracts to the oblate shape is smaller, owing to the higher initial bubble overpressure, thus resulting to a thicker jet and, eventually, a larger satellite bubble. This is

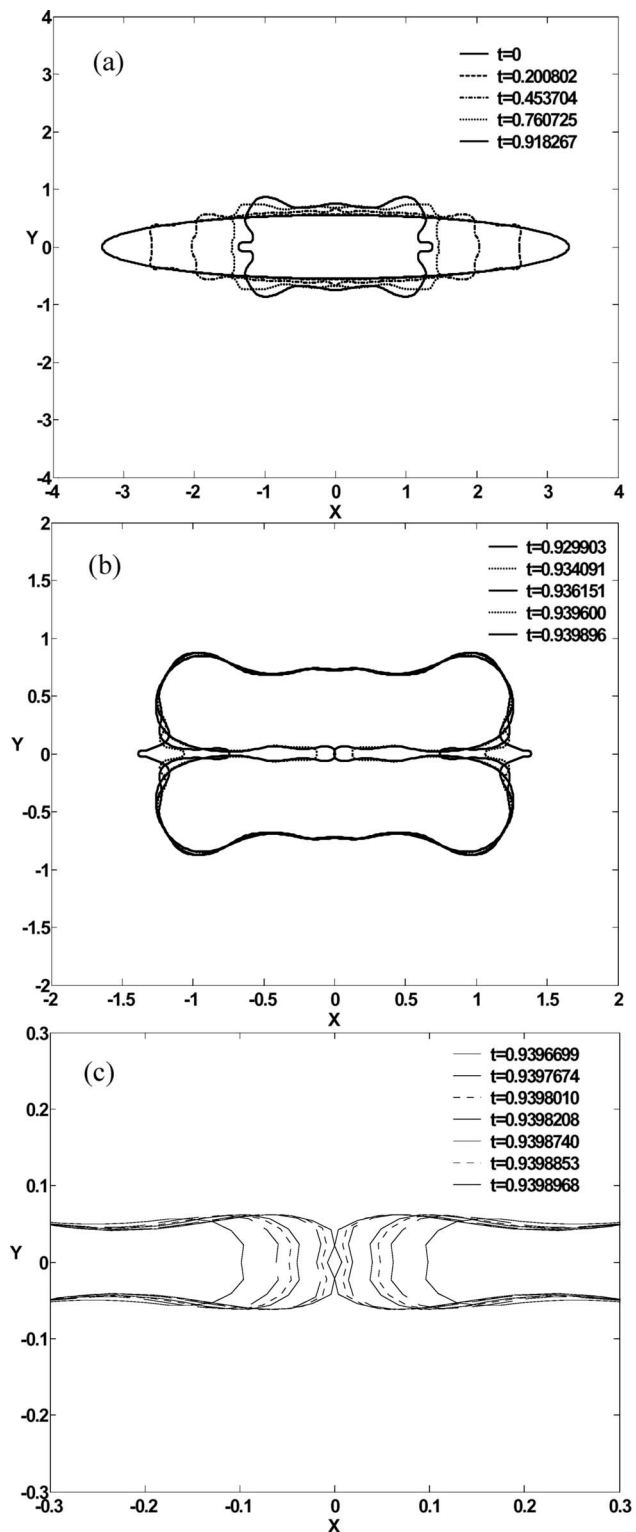


FIG. 13. Time evolution of the shape of the bubble (a) in the beginning of the motion, (b) during jet formation, and (c) during collapse;  $S=0.55$ ,  $P_{St}=4.1$ , infinite  $Oh^{-1}$ , with 130 elements in the region  $0 \leq \theta \leq \pi/2$ .

clearly illustrated in Figs. 16(a)–16(c) that show the evolution of bubble shapes for inviscid oscillations with  $S=0.6$  and  $\varepsilon_B=0.05$ . For such small values of  $\varepsilon_B$  the overall pattern of dynamic behavior does not change with the exception of  $Oh_{Cr}^{-1}$  that now increases as a manifestation of the stabilizing influence of initial overpressure; when  $\varepsilon_B=0.05$   $Oh_{Cr}^{-1}$

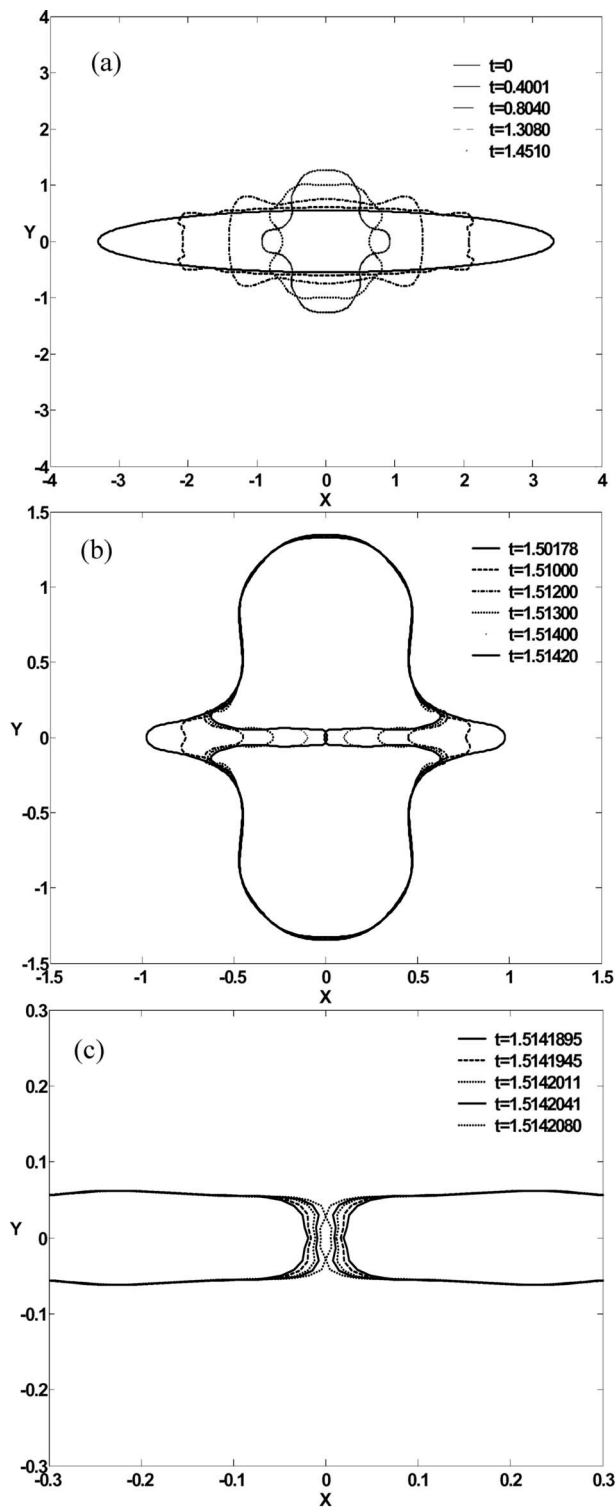


FIG. 14. Time evolution of the shape of the bubble (a) in the beginning of the motion, (b) during jet formation, and (c) during collapse;  $S=0.55$ ,  $P_{St}=4.1$ ,  $Oh^{-1}=1000$ , with 130 elements in the region  $0 \leq \theta \leq \pi/2$ .

$\sim 1000$ . The pattern that was identified in the above, regarding the scaling law relating the minimum distance between coalescing jets with the time to coalescence,  $D^{3/2} \sim t$ , is recovered and holds even for very large yet finite values of  $Oh^{-1}$ . Further increase of  $\varepsilon_B$  affects the dynamics of bubble

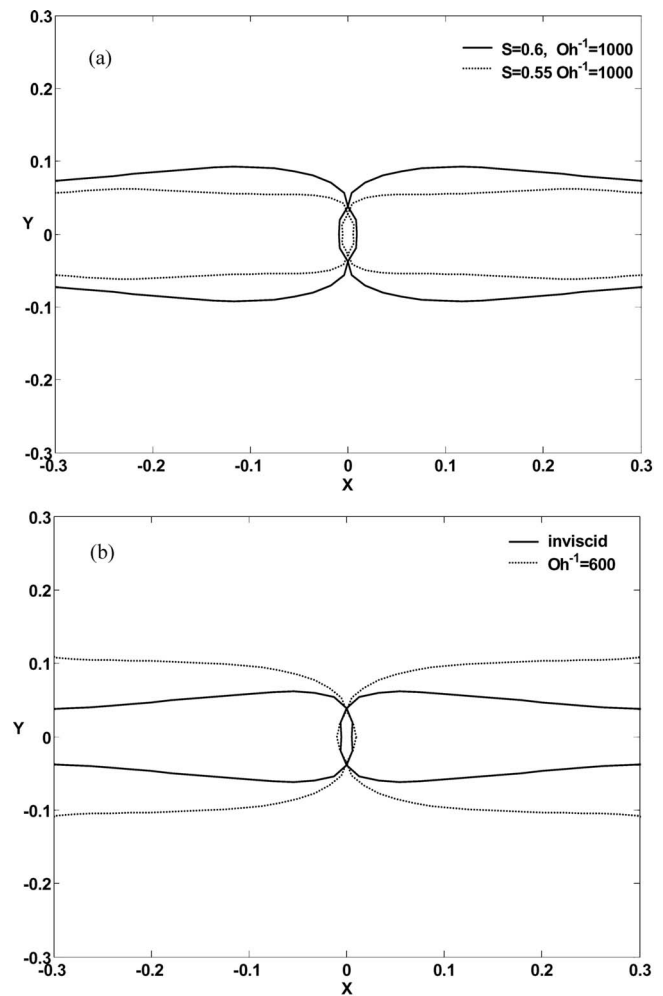


FIG. 15. Comparison of jet thickness and bubble size with (a) increasing initial elongation,  $S=0.6$  and  $0.55$ ,  $Oh^{-1}=1000$  and (b) increasing viscous effects,  $Oh^{-1}=\text{infinite}$  and  $600$ ,  $S=0.6$ .

breakup more drastically enriching the possible collapse mechanisms.

The effect of asymmetry in the initial elongation was also investigated, by imposing the types of shapes that are portrayed in Fig. 1. In this case the regions around the two poles are moving at a different speed, due to the difference in radius of curvature, with the one with the smaller radius moving faster. Once the shape of the bubble becomes roughly oblate these two regions perform out of phase oscillations until a jet is formed at the north pole, that moves along the axis of symmetry, penetrates the bubble and hits the opposite side of its interface forming a satellite and a larger toroidal bubble. This is illustrated in Figs. 17(a)–17(c) for the case with  $k=1.2$ ,  $Oh^{-1}=800$ , and the same initial elongation,  $\ell=2/(0.6)^2$ , as for an ellipsoidal bubble with  $S=0.6$ . In this case the satellite bubble does not occupy the region at the intersection between the equatorial plane and the axis of symmetry. Rather, it appears off the equator, as the two dimples that are formed symmetrically with respect to the axis of symmetry on the rounded end of the penetrating jet touch upon the opposite side of the bubble. As the level of initial asymmetry decreased the bubble was seen to collapse closer to the equatorial plane.

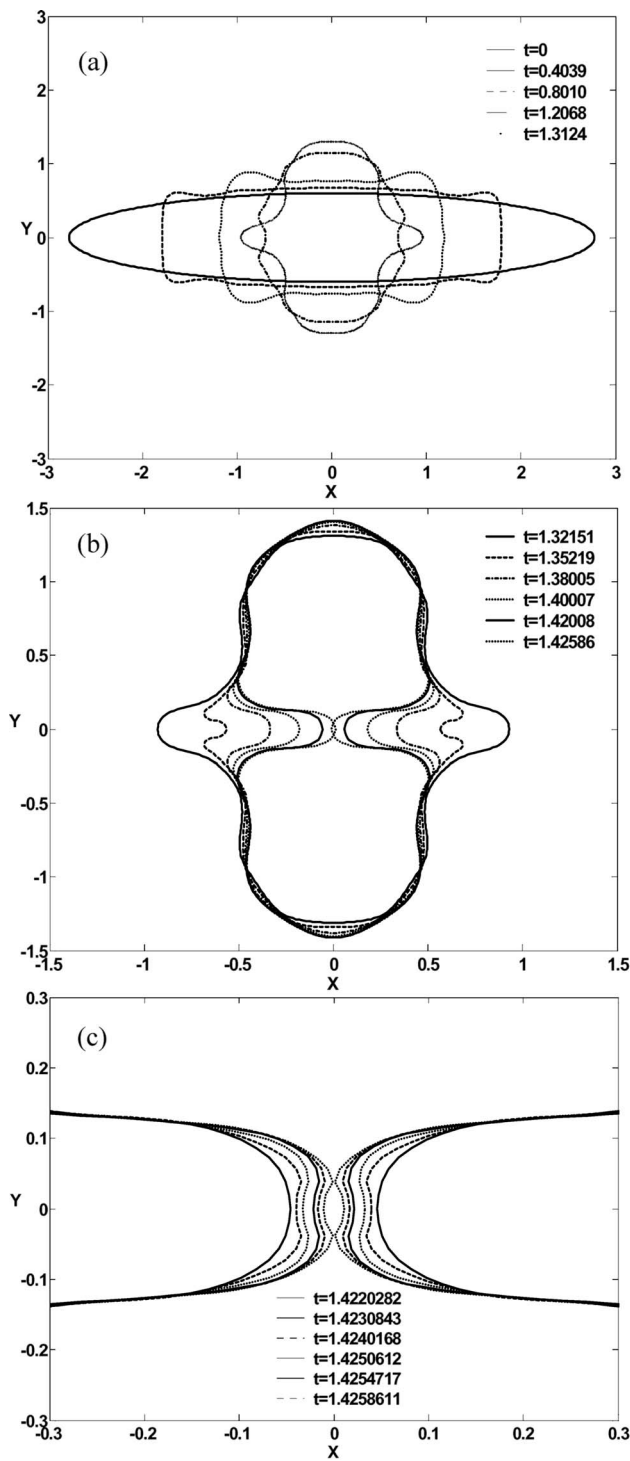


FIG. 16. Time evolution of the shape of the bubble (a) in the beginning of the motion, (b) during jet formation, and (c) during collapse;  $S=0.6$ ,  $P_{St}=4.1$ , infinite  $Oh^{-1}$ ,  $\varepsilon_B=0.05$ , with 100 elements in the region  $0 \leq \theta \leq \pi/2$ .

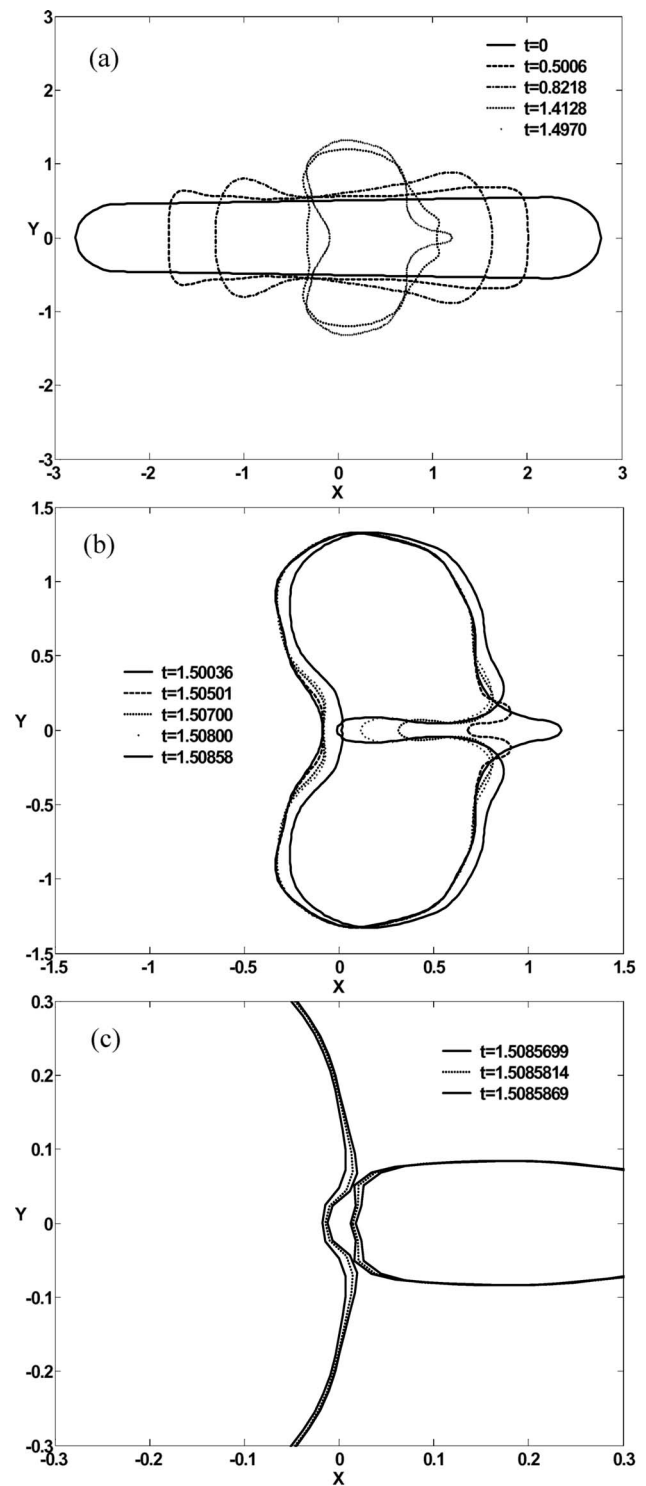


FIG. 17. Time evolution of the shape of an asymmetric bubble (a) in the beginning of the motion, (b) during jet formation, and (c) during collapse;  $P_{St}=4.1$ ,  $Oh^{-1}=800$ ,  $k=1.2$ ,  $\ell=5.55$ ,  $\varepsilon_B=0$ , with 150 elements in the region  $0 \leq \theta \leq \pi$ .

## V. CONCLUSIONS

The effect of initial elongation on the dynamic behavior of a bubble that is suspended in a liquid at atmospheric pressure is investigated. The particular case of an air bubble suspended in water was simulated extensively and it was shown that beyond a certain range of initial elongations,  $S \leq 0.6$ , the long time configuration of the bubble is either spherosym-

metric,  $Oh^{-1} < Oh_{Cr}^{-1}$ , or collapsed consisting of a small satellite bubble occupying the region around the center and a larger toroidal bubble. The collapse mechanism is quite interesting and is characterized by the formation of two counter-current jets penetrating the bubble from opposite ends and meeting at the equatorial plane. As they approach each other

their ends become rounded and two dimples appear on each one of them that are symmetrically located with respect to the axis of symmetry. The final stages of coalescence of opposite facing dimples are governed by the balance between capillary and inertia forces responsible for the pinch-off process of liquid drops and jets. In fact, the  $3/2$  scaling law describing the evolution of the minimum distance between approaching dimples against the time to pinch-off was recovered for the inviscid case and large initial elongations,  $0.55 \leq S \leq 0.6$ , and was seen to be roughly valid for large values of  $Oh^{-1}$ . A small amount of initial overpressure was shown to stabilize the bubble by increasing the value of  $Oh_{Cr}^{-1}$ . For the case of a micrometer-size air bubble suspended in water  $Oh^{-1}$  is not very large and consequently the theory presented here predicts that the bubble will eventually return to the spherically symmetric configuration. Nevertheless, as the size of the bubble increases  $Oh^{-1}$  and  $P_{St}$  both increase and it is seen that for an initial elongation characterized by  $S=0.6$ , a bubble with equilibrium radius on the order of 5 mm which amounts to  $Oh^{-1} \sim 600$  and  $P_{St} \approx 3500$ , eventually collapses in the manner described above. In other words larger bubbles are more susceptible to collapse. In fact, it was found that when  $P_{St}=3600$ ,  $S=0.6$  and  $\varepsilon_B=0$  the threshold value above which the bubble collapses is  $Oh_{Cr}^{-1} \sim 300$ . It should also be pointed out that the combination of large initial elongations and substantial internal overpressures may extend the range over which the dynamic phenomena that were identified in the present study will manifest themselves. Larger initial overpressures are also expected to modify the long-term dynamics and probably give rise to different breakup mechanisms. This process is very important in the physics of sonoluminescence and will be investigated separately in a future article.

## ACKNOWLEDGMENT

K.T. wishes to acknowledge the IKY Government Scholarship Foundation of Greece for financial support during this work.

<sup>1</sup>J. W. Strutt (Lord Rayleigh), "On the pressure developed in a liquid during the collapse of a spherical cavity," *Philos. Mag.* **34**, 94 (1917).

- <sup>2</sup>M. S. Plesset, "The dynamics of cavitation bubbles," *J. Appl. Mech.* **16**, 228 (1949).
- <sup>3</sup>C. D. Ohl, T. Kurz, R. Geisler, O. Lindau, and W. Lauterborn, "Bubble dynamics, shock waves and sonoluminescence," *Philos. Trans. R. Soc. London, Ser. A* **357**, 269 (1999).
- <sup>4</sup>R. Geisler, "Untersuchungen zur Laserinduzierten Kavitation mit Nanosekunden—Femtosekundenlasern," Ph.D. thesis, University of Goettingen, Germany (2004).
- <sup>5</sup>J. Eggers, "Universal pinching of 3D axisymmetric free surface flow," *Phys. Rev. Lett.* **71**, 3458 (1993).
- <sup>6</sup>D. Leppinen and J. R. Lister, "Capillary pinch-off in inviscid liquids," *Phys. Fluids* **15**, 568 (2003).
- <sup>7</sup>N. A. Pelekasis and J. A. Tsamopoulos, "Bjerknes forces between two bubbles. Part 1: Response to a step change in pressure," *J. Fluid Mech.* **254**, 467 (1993).
- <sup>8</sup>T. S. Lundgren and N. N. Mansour, "Oscillations of drops in zero gravity with weak viscous effects," *J. Fluid Mech.* **194**, 479 (1988).
- <sup>9</sup>G. K. Batchelor, *An Introduction to Fluid Dynamics* (Cambridge University Press, Cambridge, 1967).
- <sup>10</sup>C. A. Weatherburn, *Differential Geometry of Three Dimensions Vols. I and II* (Cambridge University Press, Cambridge, 1927).
- <sup>11</sup>J. M. Boulton-Stone and J. R. Blake, "Gas bubbles bursting at a free surface," *J. Fluid Mech.* **254**, 437 (1993).
- <sup>12</sup>H. Lamb, *Hydrodynamics* (Cambridge University Press, Cambridge, 1932).
- <sup>13</sup>J. R. Blake and D. C. Gibson, "Cavitation bubbles near boundaries," *Annu. Rev. Fluid Mech.* **19**, 99 (1987).
- <sup>14</sup>H. N. Oguz and A. Prosperetti, "Bubble oscillations in the vicinity of a nearly plane free-surface," *J. Acoust. Soc. Am.* **87**, 2085 (1990).
- <sup>15</sup>N. K. McDougald and L. G. Leal, "Numerical study of the oscillations of a non spherical bubble in an inviscid incompressible liquid. Part I: Free oscillations from nonequilibrium initial conditions," *Int. J. Multiphase Flow* **25**, 887 (1999).
- <sup>16</sup>J. K. Choi and G. L. Chahine, "Noise due to extreme bubble deformation near inception of tip vortex cavitation," *Phys. Fluids* **16**, 2411 (2004).
- <sup>17</sup>E. Canot and J.-L. Achard, "An overview of boundary integral formulations for potential flows in fluid-fluid systems," *Arch. Mech.* **43**, 453 (1991).
- <sup>18</sup>N. A. Pelekasis, J. A. Tsamopoulos, and G. D. Manolis, "A hybrid finite-boundary element method for inviscid flows with free surface," *J. Comput. Phys.* **101**, 231 (1992).
- <sup>19</sup>J. M. Boulton-Stone, "A comparison of boundary integral methods for studying the motion of a two-dimensional bubble in an infinite fluid," *Comput. Methods Appl. Mech. Eng.* **102**, 213 (1993).
- <sup>20</sup>J. F. Thompson, Z. U. Warsi, and W. C. Mastin, *Numerical Grid Generation: Foundations and Applications* (North-Holland, Amsterdam, 1985).
- <sup>21</sup>M. Loewenberg and E. J. Hinch, "Numerical simulation of a concentrated suspension in shear flow," *J. Fluid Mech.* **321**, 395 (1996).
- <sup>22</sup>S. Abid and A. K. Chesters, "The drainage and rupture of partially-mobile films between colliding drops at constant approach velocity," *Int. J. Multiphase Flow* **3**, 613 (1994).